Petroleum Science 23 (2026) 3556–3575

Contents lists available at ScienceDirect

Petroleum Science

journal homepage: www.keaipublishing.com/en/journals/petroleum-science

Original Paper

In-situ combustion of heavy oil within a vuggy carbonate reservoir: Part II—Mechanism of permeability inversion and rock fabric transformation

Rita Fazlyeva [a], Tagir Karamov [b,*], Matthew Ursenbach [a], Roberto Aguilera [a], Andrey Voropaev [c], Mikhail Spasennykh [b], Gordon Moore [a], Alexey Cheremisin [b], Mehta Sudarshan [a]

[a] Chemical and Petroleum Engineering Department, University of Calgary, 2500 University Drive NW, Calgary, Alberta T2N 1N4, Canada
[b] Center for Petroleum Science and Engineering, Skolkovo Institute of Science and Technology, Moscow, 121205, Russia
[c] Hydroisotop GmbH, Woelkestrasse 9, Schweitenkirchen, 85301, Germany

ARTICLE INFO

Article history:
Received 9 September 2025
Received in revised form
26 January 2026
Accepted 5 February 2026
Available online 11 February 2026

Edited by Yan-Hua Sun

Keywords:
In-situ combustion
Carbonates
Dolomite reservoir
Isotope
XRD
EDX

ABSTRACT

Predicting the performance of in-situ combustion (ISC) in carbonate reservoirs is notoriously challenging. This study reveals a paradoxical permeability inversion phenomenon: initially high-permeability grainstones (up to 2600 mD) suffer catastrophic permeability damage, while initially low-permeability packstones (below 250 mD) show marked improvement. We demonstrate that this counter-intuitive behavior is driven by the thermal decomposition of dolomite. This process fundamentally transforms the rock fabric, shifting it from a robust, grain-supported architecture (grainstone/packstone) to a fragile, matrix-supported texture (wackstone-like), which critically reduces pore throat radii in high-quality rocks. At the micro-scale, the key agent of this transformation is identified as the neoformation of needle-shaped magnesium-calcium hydrosilicate crystals, which occlude pores and can occupy up to 50% of the pore volume. Stable isotope analysis confirms that this mineralogical alteration is the dominant process, revealing up to 70% of CO_2 produced originates from dolomite decomposition rather than hydrocarbon combustion. These findings prove that initial reservoir quality is a poor predictor of ISC performance; instead, the geochemical reactivity and thermal stability of the rock fabric are paramount. We therefore propose the rock-fabric number as a more robust metric for predicting reservoir response to thermal EOR processes.

1. Introduction

More than 50% of heavy oil (Akbar et al., 2000) is contained in carbonates, which are some of the most prolific and challenging reservoirs for oil recovery due to their heterogeneity caused by the complex porous media containing matrix, fractures, vugs, and karsts (Mazzullo, 2004). Air injection has immense potential for hydrocarbon recovery from various reservoirs. Depending on the oil type, it can be implemented either air only, wet combustion or in combination with other steam-based methods.

Despite multiple successful projects recovering oil from the carbonate reservoirs with the application of air-based injection methods (Miller, 1995; Turta et al., 2007), there are certain concerns related to the carbonate precipitation and fines migration that might cause permeability reduction (Hascakir and Kovscek, 2014). Recent experimental studies have confirmed that significant permeability damage can occur during thermal treatment of carbonates (Fazlyeva et al., 2023; Mogensen and Masalmeh, 2020; Tao et al., 2024), though the underlying pore-scale mechanisms are not fully understood. Conversely, thermal breakthrough from the production wells due to the existing fractures remains another major operational challenge (Fatemi, 2009).

While most of the post-burn studies in the in-situ combustion (ISC) literature are focused on the clastic reservoirs (Bennion et al., 1977; Buxton and Pollock, 1974; Hogue et al., 2015; Jha and

* Corresponding author.
E-mail address: T.Karamov@skoltech.ru (T. Karamov).
Peer review under the responsibility of China University of Petroleum (Beijing).

https://doi.org/10.1016/j.petsci.2026.02.008

Verkoczy, 1986; Perry and Gillot, 1982), less attention has been dedicated to the macro and microscopic characteristics of carbonate reservoirs (Hascakir and Kovscek, 2014). However, the interest in carbonate ISC has grown recently (Antolinez et al., 2023; Mogensen and Masalmeh, 2020; Seidy-Esfahlan et al., 2024). Current research has primarily advanced along two fronts: refining kinetic models to better capture the low-temperature and high-temperature oxidation pathways (Alizadeh, 2020; Baudin et al., 2023) and developing numerical simulations to handle the complexities of fractured systems (Askarova et al., 2025; Meng et al., 2023), and even exploring the potential of ISC for low-carbon hydrogen generation (Okere and Sheng, 2023, 2024, 2025). While some experimental works have begun to characterize mineralogical alterations, identifying dolomite decomposition and the formation of new phases as key processes at high temperatures (Karamov et al., 2024; Mukhametdinova et al., 2024). A critical gap remains in linking specific, micro-scale geochemical reactions to macro-scale changes in reservoir properties. The fundamental mechanisms that control the evolution of the pore network—leading to the paradoxical effect of permeability reduction in high-quality rock and improvement in low-quality rock—have yet to be elucidated. This study directly addresses this gap by presenting a multi-scale, rock-based investigation into the pore network transformation and dolomite decomposition during ISC.

Perry and Gillot (1982) studied mineralogical transformation as an indicator of the maximum temperature established during the field-scale implementation of ISC on the Alberta oil sands. The results demonstrated that calcite, chlorite, illite, kaolinite, dolomite, and smectite can be used to determine temperature zones between 350 and 700 °C (±50 °C). In the ISC literature, this temperature interval corresponds to the high-temperature range (HTR), where bond scission reactions occur (Moore et al., 1992). Operation in the high-temperature oxidation (HTO) is the main reaction mode in the HTR and normally contributes the most to energy generation and successful oil recovery.

A similar finding was reported by Hogue et al. (2015) based on the macroscopic observations and X-ray diffraction (XRD) analysis on the extracted core material from Alberta's AIDROH pilot project. They confirmed that smectites underwent significant changes because of dehydration at high temperatures.

The chemical reactions governing the ISC processes are complicated by their nature involving numerous ongoing endo/exothermic processes affected by multiple factors: temperature, pressure, oil composition, oxygen uptake, etc. (Alizadeh, 2020). However, the difficulty of operating or predicting the performance of ISC in carbonate reservoirs further complicates a blend of the kinetic reactions by introducing its decomposition reactions generating CO_2 making it more difficult to interpret the product gas composition and hence, gas phase combustion parameters.

During high-temperature treatments of sedimentary rocks, the mineral matrix undergoes significant transformations, particularly impacting carbonates. Among these, dolomite is one of the most sensitive minerals (Olszak-Humienik and Jablonski, 2015). Defined by temperature rise, dolomite decomposition occurs in three steps. First, at atmospheric pressure and temperatures above 300 °C, it decays to calcite and magnesium oxide with the release of carbon dioxide and mass loss of about 23% ($CaMg(CO_3)_2 \Leftrightarrow CaCO_3 + MgO + CO_2$). In the second step, above 530 °C, $CaMg(CO_3)_2$ continues transformation and decomposes into calcium and magnesium oxides and carbon dioxide ($CaMg(CO_3)_2 \Leftrightarrow MgO + CaO + 2CO_2$. The third step occurs at a temperature above 850 °C reaching a mass loss of 47.73% (theoretical maximum) when calcite completely dissociates with the CO_2 release ($CaCO_3 \Leftrightarrow CaO + CO_2$).

The partial pressure of CO_2, heating rate, experimental conditions, and sample integrity are some of the variables that might affect the dolomite dissociation (Caceres and Attiogbe, 1997; Li and Messing, 1983; McIntosh et al., 1990). Caceres and Attiogbe (1997) reported that structurally deformed dolomite dissociates at temperatures approximately 100 °C lower compared to similar processes in consolidated matrices. In the study conducted by Li and Messing (1983) under the N_2-CO_2 environment, they described that the addition of chloride salts causes a temperature reduction, under which dolomites start decomposing.

While the complexities of ISC in carbonate reservoirs are acknowledged, a detailed, rock-based understanding of the coupled geochemical and petrophysical transformations remains a critical knowledge gap. This study addresses this gap by presenting a comprehensive post-burn analysis of dolomite cores subjected to ISC. Building upon the experimental framework detailed in Part I of this study (Fazlyeva et al., 2023), we employ a multi-scale suite of analytical techniques—from macro-scale imaging to micro-scale SEM/EDX and stable isotope analysis—to elucidate the mechanisms of mineral alteration, identify neo-formed phases, and quantify their impact on the pore network, rock fabric, and permeability. The objective is to provide a crucial link between microscopic chemical reactions and the evolution of macroscopic reservoir properties, offering new insights for optimizing and predicting ISC performance in dolomitic reservoirs.

2. Materials, methods, and post-combustion procedures

The core material used in this study consisted of Silurian-aged outcrop dolomite samples, purchased from Kocurek Industries Inc. (Caldwell, Texas, USA). This rock type was selected as a representative analogue for vuggy carbonate reservoirs. All experiments described herein are laboratory-scale combustion tests designed to simulate the in-situ combustion process under controlled conditions, not an analysis of core from a field application.

The thermal decomposition of carbonates has a significant impact on ISC recovery that must be considered, as it affects various aspects of the process from the nature of kinetic reactions (Hascakir and Kovscek, 2014; Pope et al., 2020; Shojaiepour et al., 2014) to the material balance calculation (Jiang et al., 2020). Therefore, a preliminary screening was conducted to ensure the selected outcrop material closely matched the mineralogy of the target reservoir. A series of XRD experiments were performed on nine different outcrop samples (labeled A–I in Fig. 1) to identify the one with the mineral composition closest to a typical dolomite

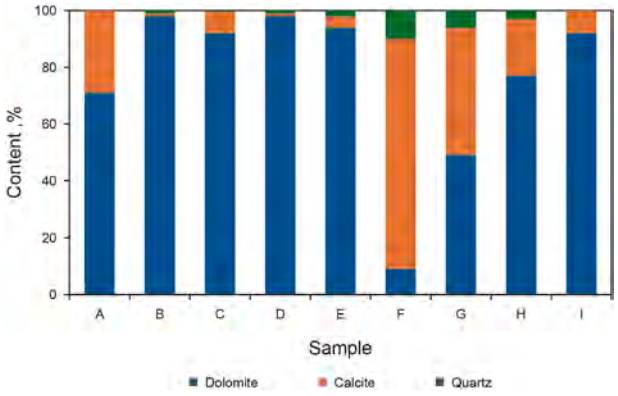

Fig. 1. Mineral composition (XRD) of the core samples used for the selection of the sample that will represent the original core.

reservoir rock. Based on this analysis, Sample H was selected for all subsequent experiments due to its high dolomite content (over 70%), which is representative of the target reservoir type. Sample A in Fig. 1, for reference, represents the mineralogical composition of an actual core from the target field, containing 71.2% dolomite, 28.6% calcite, and 0.2% quartz. The selected Sample H is the closest analogue to this benchmark.

To evaluate the pore space structure of the core plugs and the remaining residual inclusions, a GE Phoenix V|tome|x L240 micro-computer tomography scanner was used with a resolution of 30 μ/voxel. To determine the parameters of the pore space, the obtained 3D images were segmented using the GeoDict software of MathToMarket, and parallelepiped voxels of 11003–13003 were used for the calculations. The volume of the analyzed structures is 11–46 mm^3.

Scanning electron microscopy (SEM) was employed for detailed microstructural investigation of rock samples both before and after the combustion tube (CT) experiment. The analyses were conducted using a Thermo Fisher Scientific Quattro S SEM, which accommodates small rock samples (~5 mm in size) chipped off from cores. The electron beam current ranged from 1 pA to 200 nA, with an accelerating voltage between 200 V and 30 kV. The highest spatial resolution achieved was 5 nm. Both secondary electron (SE) and backscattered electron (BSE) imaging modes were utilized during scanning at an accelerating voltage of 10–15 kV (Erdman and Drenzek, 2013). The resulting images had a resolution of 1.536 × 1.094 pixels.

For semiquantitative elemental composition analysis, an integrated energy-dispersive X-ray spectrometer (EDX; Quantax, Bruker, USA) was used. Lithotyping, structural analysis, and void space characterization were conducted on thin sections using an AxioScope 5 petrographic microscope (ZEISS, Germany), following the Dunham classification system (Dunham and Ham, 1962).

The isotopic composition of carbon, hydrogen, nitrogen, and sulphur in rocks, gases, oils, and water was analyzed using GC-IRMS and EA-IRMS systems. GC-IRMS enabled compound-specific isotope analysis through chromatographic separation, followed by oxidation or pyrolysis at high temperatures (960 or 1400 °C) and mass spectrometry. EA-IRMS facilitated bulk isotope measurements by combusting or pyrolyzing samples encapsulated in tin or silver foil at 1020 or 1400 °C, with the resulting gases (CO_2, N_2, SO_2, H_2) separated chromatographically before isotopic analysis. Calibration was performed using international standards, including NBS 22 for carbon and hydrogen and IAEA N_2 for nitrogen, with results recalculated relative to international reference scales such as PDB, SMOW, AIR, and CDT. Carbonate carbon isotopes were measured after acid treatment of rock samples with phosphoric acid, while organic carbon isotopes were analyzed post-acid washing. Isotopic measurement precision was ±0.2‰ for carbon, ±0.5‰ for nitrogen and sulphur, and ±1.5‰ for hydrogen. For EA-IRMS analysis, sample aliquots of 0.2–1.0 mg for oil and 0.5–5.0 mg for bulk rock were used. For carbonate-specific analysis, rock powder samples of approximately 0.3 g were reacted with phosphoric acid. A total of 5 rock samples, 5 gas samples, and 7 oil samples were analyzed as part of this study. To ensure analytical reproducibility, each sample was analyzed multiple times (in triplicate), and the average values are reported in the results.

To evaluate reservoir properties of the post-combusted dolomites, a series of helium permeability and porosity measurements were conducted using an AP-608 automated permeameter/porosimeter manufactured by Coretest Sytems. Due to its core holder size limitation, neither the permeability nor porosity of the core plugs used for the CT experiments was possible to measure. Thus, every core plug was represented with a cylindrical miniature core plug length and diameter which were 37.7 and 51 mm, respectively. The miniatures were collected from the same bed of the outcrop and were assumed to have similar properties as their larger analogs.

2.1. Triple-porosity model concept

To mimic real reservoir conditions with severe heterogeneity, a triple-porosity model was chosen: porosity of matrix, fracture, and vug. A detailed description of the experimental setup and procedure was described in the first part of this study (Fazlyeva et al., 2023).

Two types of fractures can be distinguished in this current study. The first one is the crushed dolomite surrounding the core plugs as it has significantly higher permeability values in comparison with the consolidated matrices of the core plugs. Another type of fracture is characterized by the gap between the two parts of the customized core plug: the vug part, and the cap of the core plug itself. Finally, the third type of porosity is presented by the artificially created vug as well as naturally formed vugs during carbonate dissolution.

2.2. Analyses of crushed cores and core plugs: residual saturations

Following the combustion tube experiment, the apparatus was carefully disassembled to analyze the post-burn material. The packed core, which consisted of the dolomite material selected during the initial screening process (analogous to Sample H in Fig. 1), was extracted in sequential segments along the length of the tube, from the production end to the injection end. This segmentation allowed for a detailed analysis of the residual saturations and coke deposition as a function of the distance and maximum temperature reached.

The samples listed in Table 1 (e.g., Core 1-1, Core 2-1, etc.) represent these consecutive segments of crushed dolomite extracted from the combustion tube. Each segment was subjected to a loss on ignition (LOI) test to quantify the amount of coke. During the LOI test, all the core samples placed in the crucibles were heated at 600 °C for 16 h. After cooling the samples, they were placed in a desiccator and later weighed. Any mass loss greater than the one observed in the blank test was assumed to be coke. Table 1 shows that some of the samples exceeded 20%, which has been often observed in dolomite samples.

Due to the nature of the packed core, it is impossible to distinctively separate the crushed core from the frac sand as some of the carbonate grains were mixed with and transported to the frac sand and vice-versa. Thus, in reporting the mass loss of the crushed core, the frac sand is also added to the balance, however, it was considered as a non-reactive material and all the losses were related to carbonates only.

Core plugs 1 and 3 were dry-cut in half using a diamond saw. Half of each plug was kept for further visual observation and the other half was crushed and extracted similar to the crushed core pack post-test material to measure the post-test hydrocarbon and water saturation. The coke amount was identified through the LOI test.

Table 2 demonstrates the mass changes of core plugs, maximum temperatures, and saturations before and after the experiment. The average mass loss from the crushed consolidated core material was approximately 4%.

While conducting the CT test and examining the results, it was observed that a substantial quantity of CO_2 was generated in the gaseous phase, surpassing the amount that was anticipated from the combustion reactions of oxygen and oil. The quantity of CO_2 created from the combustion reactions was computed using

Table 1
LOI tests on crushed core samples (from the production end to injection end).

Sample name	Crucible mass, g	Mass of crucible + sample, g		Sample mass, g	LOI, %
		Before	After		
Blank	64.6210	124.5168	119.4508	59.8958	8.46
16 frac sand	63.4564	123.3399	122.6411	59.8835	1.17
20/30 frac sand	62.2476	122.0971	121.9341	59.8495	0.27
20/30 frac sand	69.3262	128.2306	126.5892	58.9044	2.79
Core 1-1	57.1401	118.0624	108.6879	60.9223	15.39
Core 1-2	66.8172	126.6578	118.6239	59.8406	13.43
Core 2-1	71.7523	131.8173	120.1839	60.0650	19.37
Core 2-2	69.4334	129.2020	116.1797	59.7686	21.79
Core 2-3A	67.9130	127.4017	116.2703	59.4887	18.71
Core 2-3B	63.4533	122.9364	105.7232	59.4831	28.94
Core 3-1A	61.9821	121.8645	109.2957	59.8824	20.99
Core 3-1B	73.6066	132.1709	119.6480	58.5643	21.38
Core 3-2	66.6400	126.4443	118.5486	59.8043	13.20
Core 4	55.6236	115.9485	107.6544	60.3249	13.75
Core 5	71.3952	131.6271	122.2258	60.2319	15.61
Core 6	63.1638	113.4620	106.4199	50.2982	14.00
Core 7-1	64.6746	124.6748	117.3123	60.0002	12.27
Core 7-2	60.1279	120.0448	111.8314	59.9169	13.71
Core 8-1	62.6733	122.4833	111.2909	59.8100	18.71
Core 8-2	73.2911	133.6563	121.7397	60.3652	19.74
Core 8-3	57.8073	117.8986	107.4899	60.0913	17.32
Core 8-4	64.4889	124.5150	114.2713	60.0261	17.07
Core 9	70.8309	130.3181	119.3057	59.4872	18.51
Core 10	71.3937	131.5081	119.5802	60.1144	19.84
Core 11-1	63.4527	123.1846	113.2463	59.7319	16.64
Core 11-2	63.4286	123.3451	113.6582	59.9165	16.17
Core 12	70.7956	131.1670	120.6816	60.3714	17.37
Core 13	63.3140	123.5181	113.2725	60.2041	17.02
Core 14-1	60.9472	120.7860	110.6420	59.8388	16.95
Core 14-2	62.2478	122.7955	115.1539	60.5477	12.62
Core 14-3	66.5525	126.0953	116.4433	59.5428	16.21
Core 15	66.5520	126.2972	117.4064	59.7452	14.88
Core 16	68.5229	128.5950	119.5175	60.0721	15.11
Core 17	69.6403	129.5294	120.8246	59.8891	14.53
Frac sand (16 and 20/30)	62.6749	122.7242	121.5525	60.0493	1.95

Table 2
Analysis of core plugs.

	Core plug 1	Core plug 2	Core plug 3	Core plug 4
Vug contained oil?	No	Yes	No	Yes
Between thermocouples	3–4	5–6	7–8	8–9
Initial mass of a core plug (unsaturated), g	428.02	425.30	432.24	446.71
Mass of oil to saturate a core plug, g	24.74	27.47	26.19	19.40
Mass of oil in an artificial vug, g	0.00	7.38	0.00	7.53
Packed mass, g	452.76	460.15	458.43	473.64
Unpacked (post-test) mass, g	408.68	413.38	418.07	431.96
Maximum temperature measured (above/below), °C	594/658	632/629	615/577	577/617
Post-test saturation (oil, water, coke), %	0.00/0.13/0.00	ND	0.01/0.07/0.00	ND
Post-test saturation (oil, water, coke), g	0.02/0.53/0.00	ND	0.03/0.29/0.00	ND
Final core mass, g	408.13	ND	413.06	ND
Mass loss, g	19.89	12.24	14.17[a]	14.75[a]
Mass loss, %	4.65	2.88	3.28[a]	3.30[a]
Post-test saturations (oil, water, coke) immediately upstream core plug set, %	0.14/0.00/0.00	0.23/0.00/0.00	0.29/0.01/0.00	0.07/0.00/0.00
Post-test saturations (oil, water, coke) immediately downstream core plug set, %	0.07/0.00/0.00	0.00/0.03/0.00	0.01/0.02/0.74	0.02/0.00/0.00

[a] Not corrected for post-test saturations.

established gas phase parameters, and the difference was associated with the dolomite core decomposition. It was estimated that a total of 963 g of CO_2 was generated due to the decomposition reactions.

To validate the estimated quantity of CO_2 produced from the dolomite decomposition, a comparison was made between the mass of the core that was packed in the CT and the mass of the core retrieved from the post-test sample (with the water and hydrocarbon content subtracted). The difference between the two was found to be 1011 g of core. This value is consistent with 963 g of additional CO_2 produced, as measured in the gas stream. Additionally, this value is well within the margin of uncertainty in all the measurements and computations, thereby indicating that the dolomite decomposition was indeed responsible for the extra CO_2 production. Table 3 provides an overview of the core-CO_2 balance calculations.

Table 3
CO_2 analysis of the crushed core samples and core plugs.

Core sample	Mass before packing, g	Post-test mass, g	Difference, g	Percent decrease in mass, %
Crushed core plus frac sand	20279.1	19329.3	949.8	4.68
Core plugs	1732.3	1671.2[a]	61.1	3.52
Total	22011.3	21000.5	1010.8	4.59
CO_2 associated with decomposition of dolomite core materials[b]				
CO_2, L (ST))			517.4	
CO_2, g			963.2	

[a] This core plug mass accounts for the extraction of Core plugs 1 and 3, but not Core plugs 2 and 4, so this mass includes any water or hydrocarbon still associated with Core pugs 2 and 4. So the total post-test mass may be slightly lower, thereby increasing the difference slightly.
[b] The amount of CO_2 that should have been produced by the combustion reactions was calculated based on values typical of heavy oil combustion reactions. Any CO_2 over that amount was considered to be a product of the decomposition of dolomitic core materials.

3. Results and discussion

3.1. Macroscopic descriptive analysis of the post-burn samples

The post-test core samples were removed in incremental sections and photographed. Fig. 2 presents the unpacked post-burn samples with the maximum temperature values in each zone.

Some vital observations were made during the unpacking process. Generally, the compositional change can be seen from the colors varying from the originally light gray color of the crushed core (Fig. 2(d)). The photographs also show some of the zones less affected by combustion. Despite the termination of air injection after Zone 10, the next zone demonstrated successful oil displacement. Production ended between Zones 11 and 12, where the reservoir saturated with oil as well as the formation of a coke-like wall was observed (Fig. 2(e)). Most of the unrecovered oil was related to this area of the CT.

From the initial visual analysis of the crushed core samples excavated from the tube, two distinguishable colors were observed, and the identified core samples were taken for XRD analysis to identify mineral compositional changes (Fig. 3). Based on the XRD results, the light gray color from the sample taken near Core plug 2 shown in Fig. 2(b) indicates a mineral transition to calcite, while the darker gray contained dominantly dolomite material (sampled from the zone shown in Fig. 2(e)). Besides the thermal decomposition of dolomite and the formation of calcite, fluorapatite was indicated in both samples.

During the macroscopic analysis of the core plugs newly deposited matter on the surface of the vugs were detected. In the case of the core plug samples initially filled with oil, asphaltene/

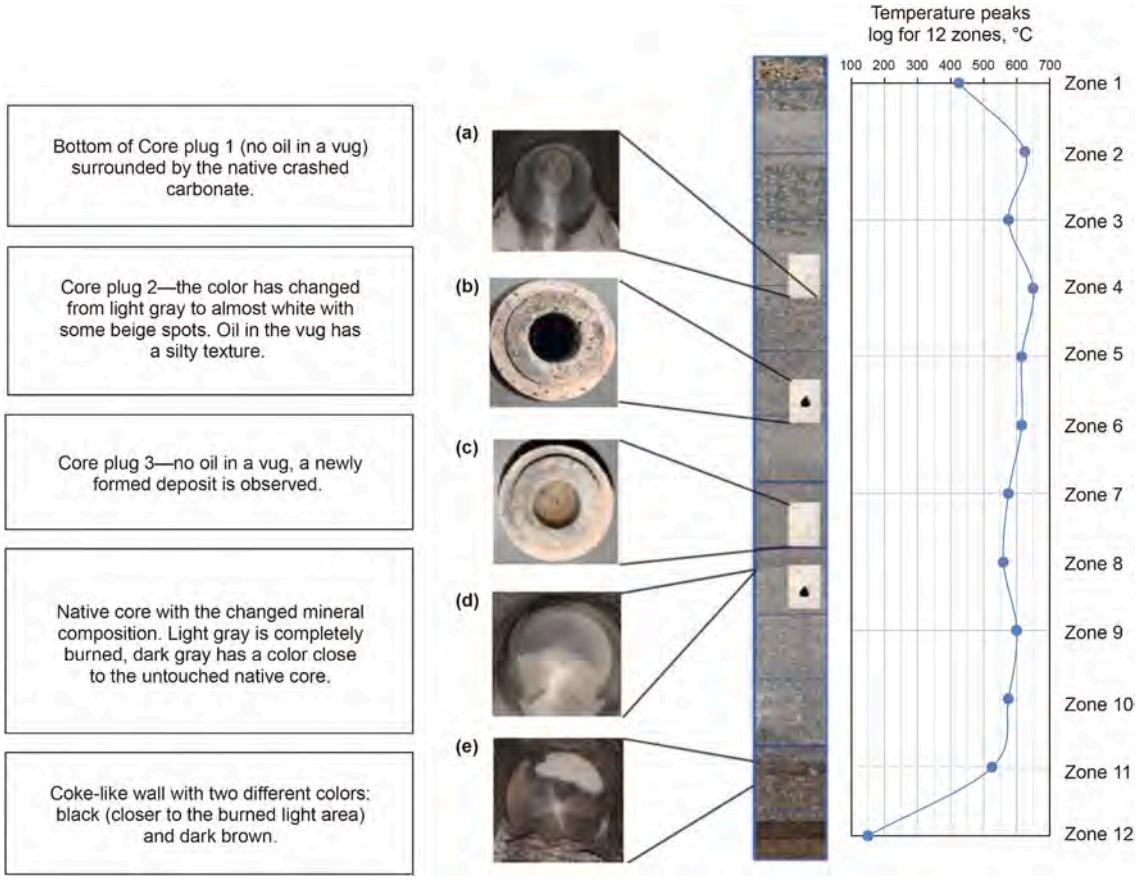

Fig. 2. Core samples including embedded core plugs with the maximum temperature log.

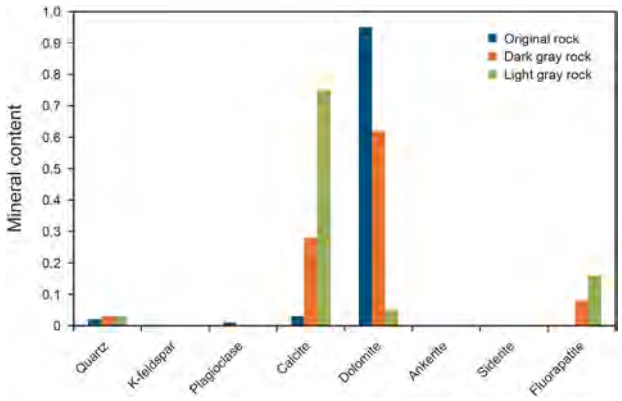

Fig. 3. Comparison of mineral composition of the original rock with the post-burn samples.

coke-like materials (Fig. 2(b)) were noticed. Examining the samples that were initially empty, a pale white precipitated material was observed in the vug, which was taken for further investigation. From the XRD analysis, it was found that two new minerals, anhydrite and perkovaite, had formed (obtained from the sample shown in Fig. 2(c)). The latter mineral is a product of the anthropogenic activity that is commonly found in the mining industry when coal is burnt (Krivovichev et al., 2010).

The formation of anhydrite was also reported by examining the samples obtained from the Sloss field in Nebraska (Buxton and Pollock, 1974). It was recognized that the newly created anhydrite crystals were a result of the pyrite decomposition at high temperatures. Despite the appearance of anhydrite in the reservoir rock, its effect on the reservoir rock properties was insignificant as the highest permeability could still be detected. This phenomenon can be explained by the observations obtained in this current work.

The mechanism of anhydrite formation, in this study, can be justified by the reaction of sulphur contained in both brine and oil with the calcium in dolomite resulting in calcium sulphate precipitation. As was visually observed, the formed minerals were not integrated into the matrix and were merely covering the dolomite surface. The precipitated matter was easily removed for the study. The cracked surface (Fig. 2(e)) could be a result of the continuous air flow that assured an unrestricted path for the connected porous network. In the current study, the pH of the post-burn brine varied between 6.98 and 7.40 (original 7.30) suggesting that the calcite formation has a thermal origination rather than acid dissolution (refer to the first part of the paper Fazlyeva et al., 2023). Fig. 4 illustrates pieces of the post-burn disintegrated Core plug 1. The left part of the cap (Fig. 4(a)) shows the location of the cap similarly to its location in the CT, and the air is injected from the top to the bottom. The thickness of the zone invaded by combustion varied from 4 to 7 mm at the outer edges which can be differentiated by the pale white color. White traces (or conduits) can be also observed in the cap and lower part of the core (Fig. 4(a, c)), which are hollow spaces represented by the footprints remaining after fossils. Those conduits could be the path that the hydrocarbons followed being displaced by air flow/combustion front advance.

Oil-filled vuggy Core plugs 2 and 4 were shipped to Skoltech for microscopic analysis studies to assess the post-combustion changes. Figs. 5 and 6 show the location of sampling for the microscopy, where images in the middle are presented in real size and the small image resolution varied between 1000 and 2000 μm to capture the details of the core texture.

In Fig. 5, in some of the images (7 and 9), a distinguishable shiny black mineral is presented, which might be pyrite. However, the exact nomenclature can only be identified through structural analysis or thin sections. Image 6 clearly shows an oxidated patch (brown area) of the core section. Overall, Core plug 2 appears "clean" with no significant residual content.

Fig. 6 demonstrates the microscopic images obtained for Core plug 4. When Core plug 4 was excavated from the CT core holder, it was tightly sealed. It appeared that most of the oil followed the path vug-matrix-fracture (from the initial location of the oil filtering through the matrix towards the end of the core transitioning to the crushed core area that represents a fracture) instead of escaping from the fracture presented by the gap between the cap and the lower part of the core plug. The center image partially demonstrates that phenomenon. Besides that, the vaporized hydrocarbons moved to the upper part of the core forming a chamber. The oil-swept zones can be justified by considering multiple phenomena: thermal expansion, viscosity reduction, and gravity. The air flow was in the top-to-down direction of the CT; therefore, the vuggy core parts were exposed to the heat wave starting from the cap and then moving to the bottom. The oil located inside of the vug first experienced thermal expansion with a decrease in viscosity, allowing for the lighter hydrocarbons to move upwards despite the opposite direction of the air flow. As the combustion front continued propagating downwards, gravity drained the oil in the downward direction.

Even though the flow within the "triple porosity" model did not travel through the matrix to the crushed core area (as the additional oil added inside the vug did not leave the matrix), however, it was just a matter of time and continuous air injection to satisfy that criteria as the oxygen diffusion rate has a different

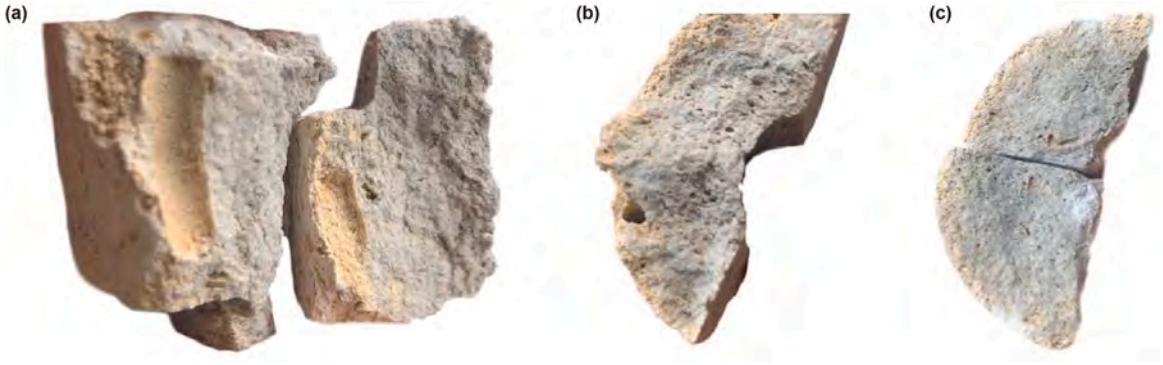

Fig. 4. Pieces of Core plug 1. (**a**) Profile of the cap; (**b**) near-vug area (bird's eye view); (**c**) the lower part of the core below the vug (bird's eye view).

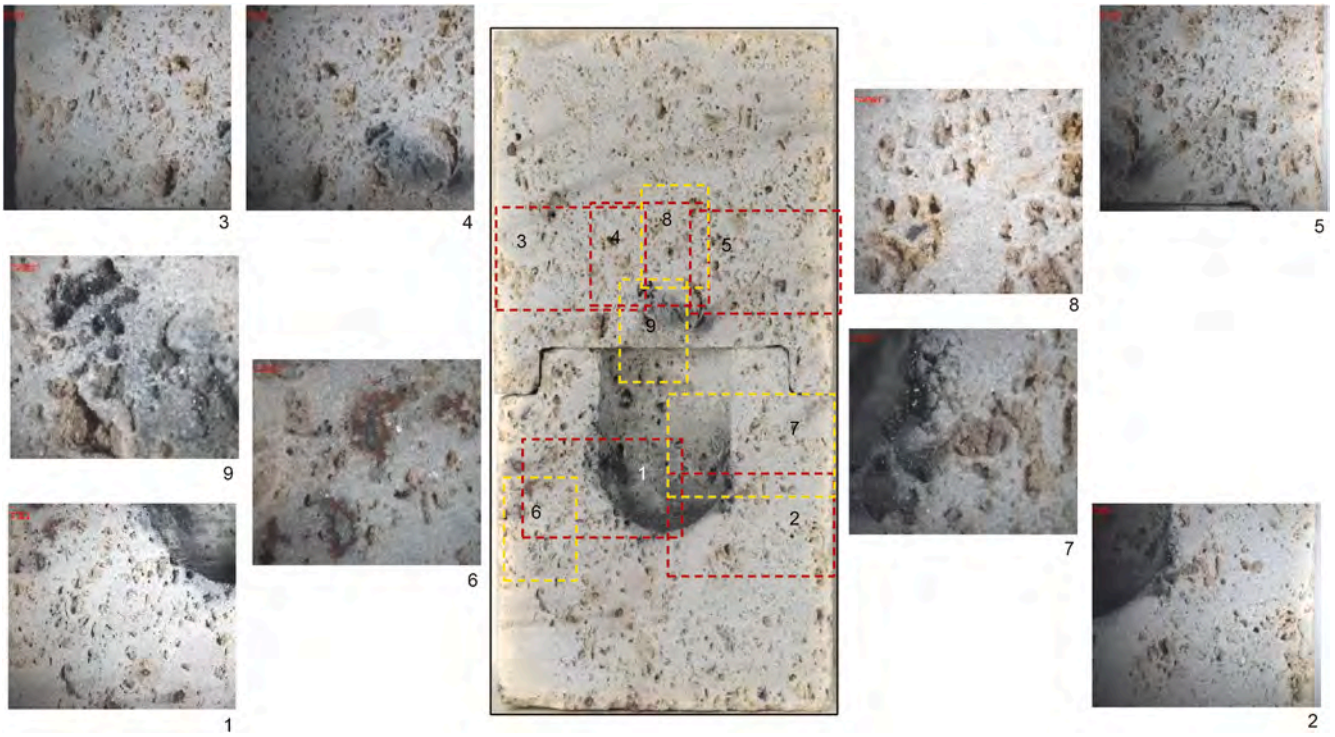

Fig. 5. Microscopic and macroscopic (center) images of Core plug 2 with the vug (oil-filled).

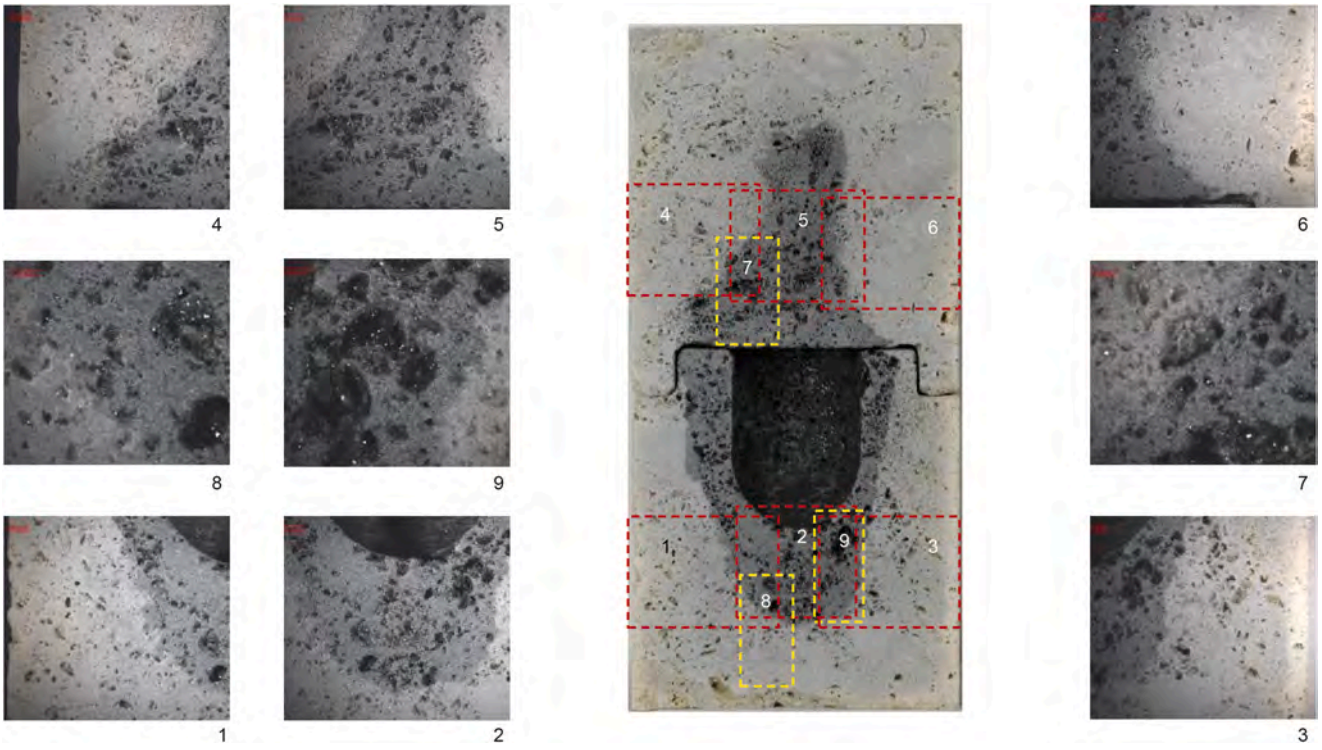

Fig. 6. Microscopic and macroscopic (center) images of Core plug 4 with the vug (oil-filled).

time scale when compared to the combustion propagation. Thus, Fig. 6 demonstrates that an air-based recovery technique has the potential to involve the oil trapped in the vugs in the production not only through the fracture conductivity but also through the matrix.

3.2. Micro-computed tomography (CT)

As the original core plugs used for the CT study were too large for some of the experiments described further, 1-inch by 1.5-inch miniature core plugs collected from the same part of the layer of

the outcrop were used and assumed to closely represent the actual core plugs. The locations of Core plugs 2 and 4 (oil-saturated vugs) used for this analysis are shown in Fig. 2.

Figs. 7 and 8(a–c) depict the core plugs scanned perpendicularly in 3D with a resolution of 30 μ/voxel. In this study, the limitation of the direct analysis is the pore structure smaller than 45–60 μm. A significant part of the pores in the carbonate rocks may be less than this limit, but this approach allows for an overall assessment of the heterogeneity of samples, phase composition, and the presence of fractures. At the same time, the total porosity value determined from tomography data with this resolution may differ significantly from that measured using the gas porosimeter. In addition, the analysis of the open/closed pores may also not reflect the coherence of a significant part of the pores due to the limitation of their minimum size. For a more accurate analysis of porosity, it is necessary to image at a higher resolution on smaller samples (mini cores) with a diameter from 25 mm and less, up to 2–8 mm.

In Figs. 7 and 8, micro-CT results exhibit the sides of Core plugs 2 and 4 in different projections. Different types of porosity, white mineral inclusions (probable pyrite) along with residual oil (shown in a gray color that occupies about 1/3 of the vug volume) can be observed in Fig. 7. The lower part has a cavity with a diameter of about 20 mm and a depth of about 25 mm. According to the results, the material is represented by two phases—the main phase and denser inclusions (on tomography: lighter, whiter) in a small amount. The pore space is heterogeneously distributed—there are both dense areas with a low porosity value and areas with sufficiently developed porosity. The size of the pores is represented from sub-resoluble and unresoluble pores (less than 30 μm) to macroscopic pores/caverns a few millimetres in size. In the vug of the sample, a low-density porous formation (coke) is observed.

The textures of the coked oil located inside the vugs were different. While Core plug 2 contained a black matte powder-like texture, Core plug 4 (Fig. 8) was characterized by a similar texture mixed with the glassy oily texture that was also observed on the walls and surface of the bottom part containing a vug.

The core miniatures were also studied using a micro-CT scan. Even though it was assumed that the miniatures veraciously represent their bigger versions, an interesting observation was obtained from the miniature similar to Core plug 4. Fig. 9 shows a stylolite joint, a common feature of carbonate rocks. However, the greater core plug did not confirm the same finding.

To determine the parameters of the pore space, the obtained 3D images were segmented using the GeoDict software of MathToMarket, and parallelepiped voxels of 11,003–13,003 were used for the calculations. The volume of the analyzed structures is 11–46 mm^3. The results of calculating the total porosity are presented in Table 4.

It should be noted that the calculation does not consider the porosity below the spatial resolution limit, so the real porosity values are expected to be higher. Moreover, the division into the open and closed porosity was not possible to perform. Part of the porosity obtained in segmented images may not have coherence and may not be determined by experimental examination (porosimetry).

Fig. 10 shows the pore distribution of Core plugs 2 and 4 and their miniatures in their actual sizes. The red color presents an empty pore space as well as traces of fossils.

GeoDict software used for the calculation of the pore distribution by size is based on the method of embedded spheres, in which the largest sphere that fits at the pore is taken as the diameter of this pore. In this analysis, the distribution of pores by size includes the pore throats and their diameters. The distribution takes into account both types of pores: open and closed.

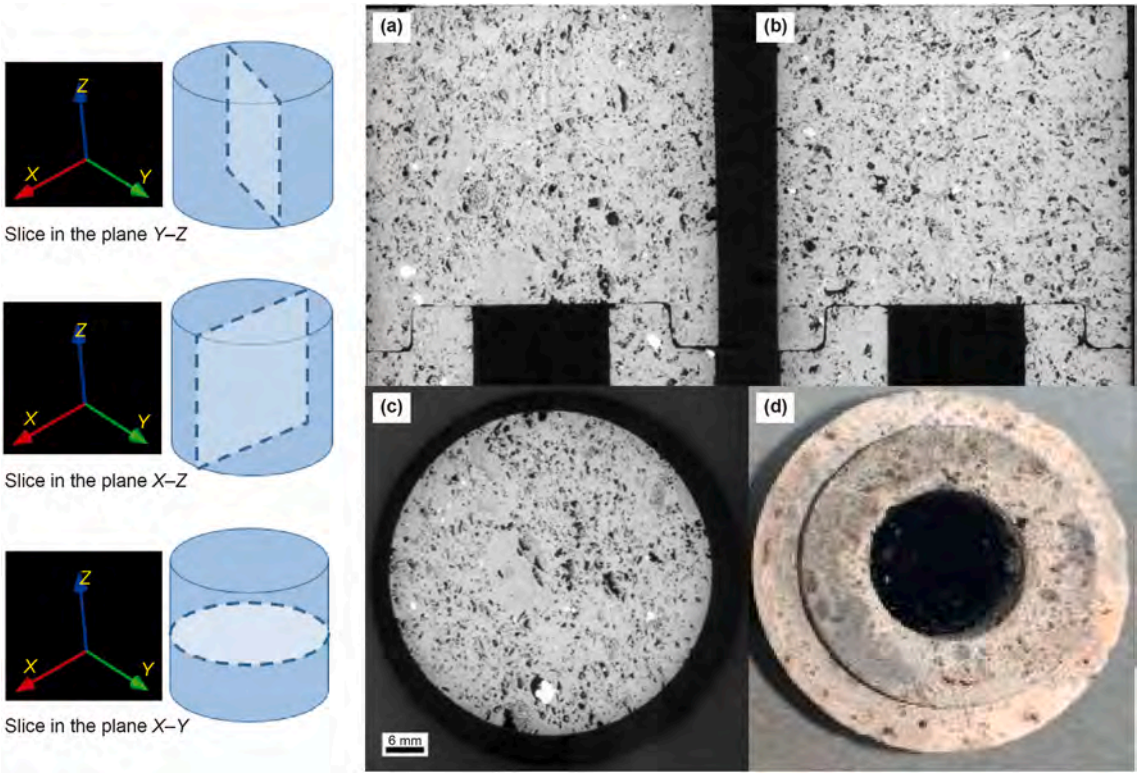

Fig. 7. Micro-CT analysis. (**a**) Plane *Y–Z;* (**b**) plane *X–Z;* (**c**) plane *X–Y;* (**d**) photography of Core plug 2 containing oil.

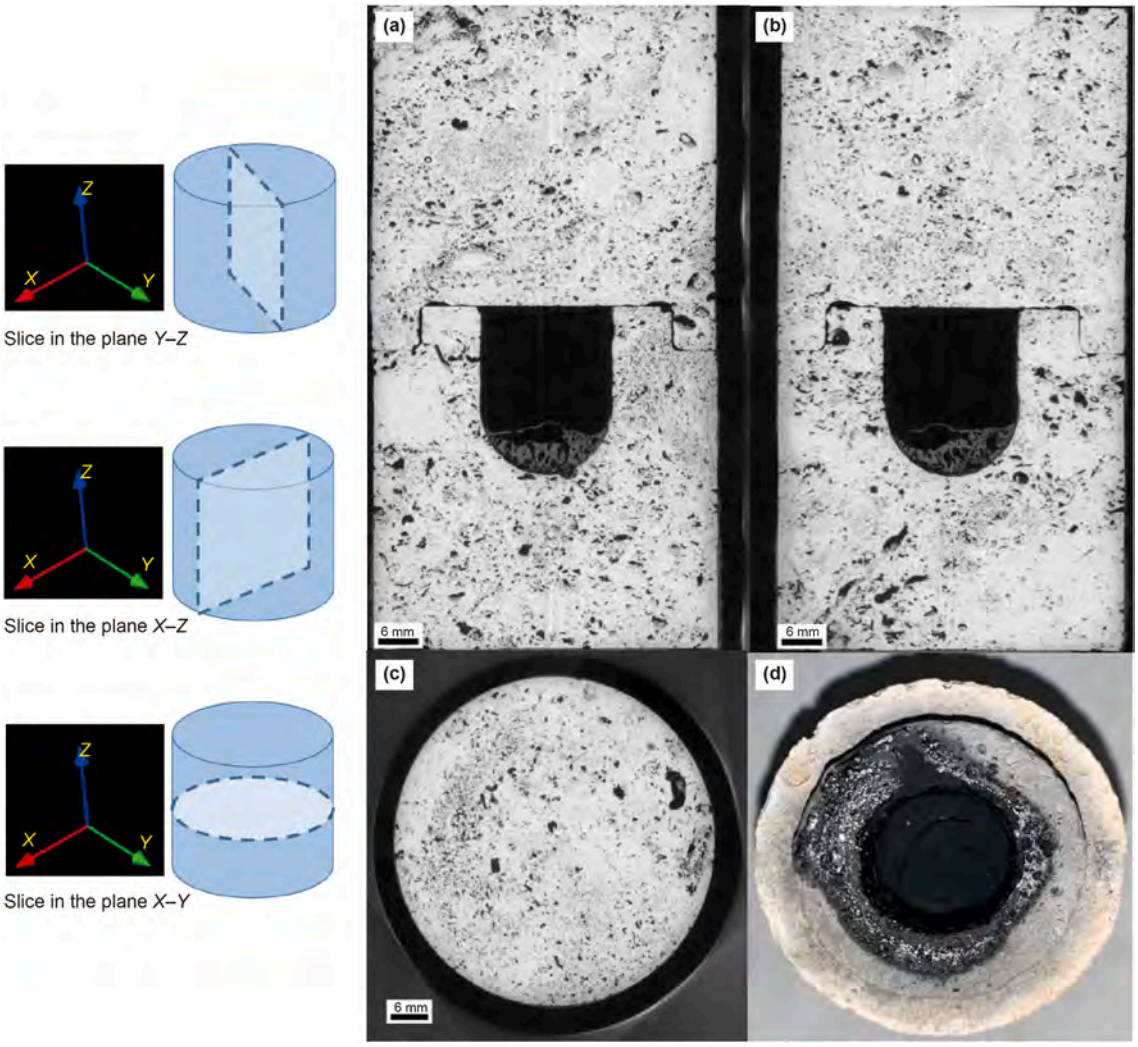

Fig. 8. Micro-CT analysis. (**a**) Plane *Y–Z;* (**b**) plane *X–Z;* (**c**) plane *X–Y;* (**d**) photography of Core plug 4 containing oil.

Differential pore distributions based on the sizes of the examined areas of the samples studied are presented in Fig. 11. It should be noted that the data acquisition size of the miniature and core plugs samples was 20 and 30 μm/voxel, respectively.

It is obvious that the pore distribution of different diameters (big or small) of the core plugs plotted with their miniatures follow similar trends and the deviation is insignificant. This emphasizes the competence of the core plugs vs their miniatures comparison.

3.3. Scanning electron microscopy (SEM)

Fig. 12 shows the initial state of the rock, which is characterized by crystalline dolostones with grain sizes ranging from 0.1 to 0.2 mm. The porosity is predominantly intercrystalline, with pore sizes between 0.01 and 0.1 mm, along with larger vugs measuring from 0.3 to 1.0 mm, evenly distributed throughout the rock. The edges of the dolomite crystals remain intact (indicated by arrows), and no minerals other than dolomite are observed (Fig. 13).

The microstructure and mineralogical composition of the samples after the experiment were analyzed using scanning electron microscopy (SEM) equipped with EDX, thin sections, and XRD techniques. The results of XRD analysis revealed that the samples remained predominantly composed of dolomite (approximately 97%–98%), with minor amounts of anhydrite (2%–3%) observed in samples 17 and 19.

The examination of thin sections indicated the widespread formation of thin organic matter layers on the rock surfaces and the partial filling of individual vugs with organic matter (Fig. 14), which might be residual coke after the experiment.

SEM analysis revealed significant alteration in the newly formed minerals and the grain structure of the rock (Fig. 15). The crystal surfaces became noticeably rough, with the formation of anhydrite as inclusions and as aggregates filling pore spaces (Fig. 15(a, b), the destruction of the initially smooth edge of dolomite (Fig. 15(c)), the rough surface of crystals resulting from the almost complete transformation of dolomite crystals (Fig. 15(d)), and numerous needle-shaped crystals (Fig. 15(e–g)). These crystals were newly formed and such minerals were not observed in the initial samples. The needle-shaped crystals measured up to 20 μm in length and approximately 0.5 μm in thickness, filling up pore space. These newly formed crystals were found exclusively in void spaces, often occupying 20%–30% of the pore volume, with some cases reaching up to 50%. Their exclusive presence in pore spaces suggests that their formation is closely

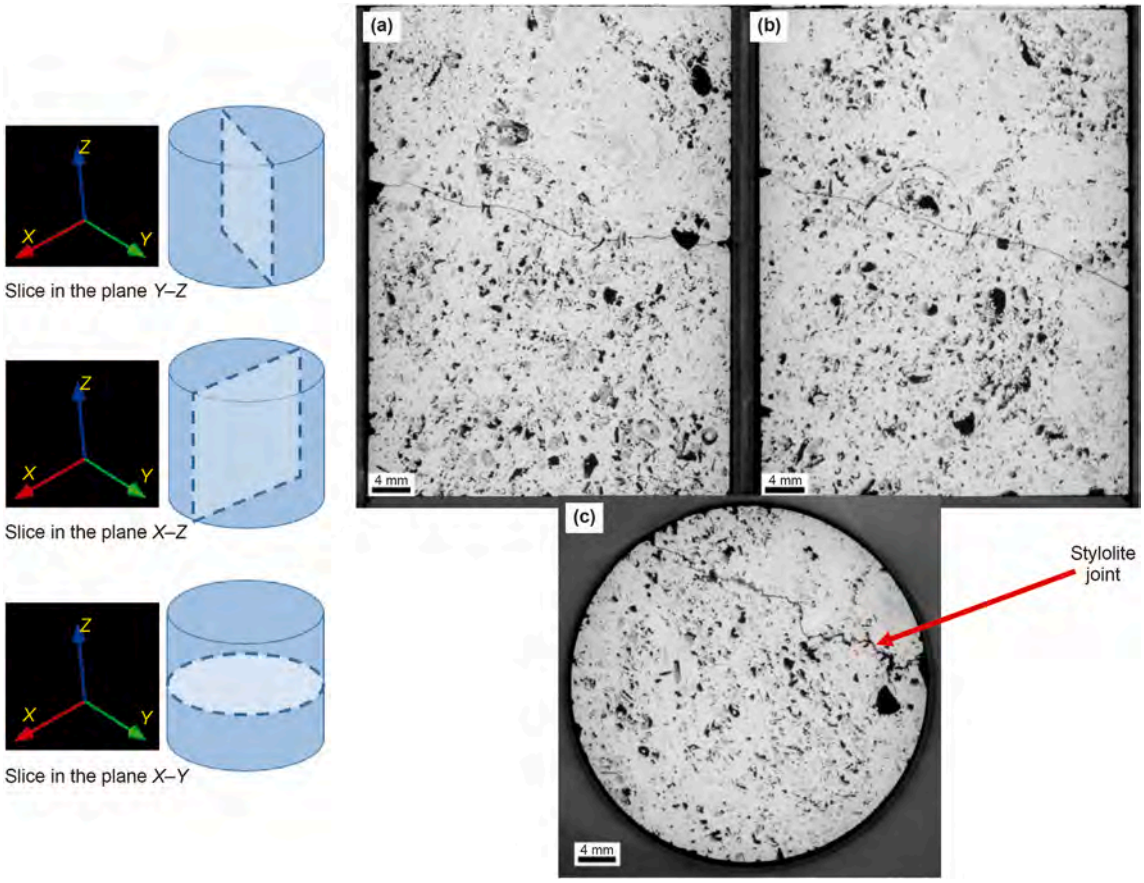

Fig. 9. Micro-CT analysis. (**a**) Plane *Y–Z;* (**b**) plane *X–Z;* (**c**) plane *X–Y* of the miniature Core plug 4.

Table 4
Total porosity results.

Sample	Total porosity, %
Core plug 2	14.19
Core plug 4	11.51
Miniature 2	10.75
Miniature 4	12.68

linked to fluid-related processes, such as changes in fluid composition, temperature, pH, and filtration-related transport within the void spaces.

EDX analysis confirmed anhydrite formation and indicated that the needle-shaped crystals primarily consist of calcium, oxygen, and silicon, with occasional traces of magnesium (Table 5). For instance, in Fig. 14, at point 5, the detected crystals were predominantly composed of Ca, Mg, Si, and O. The overall chemical

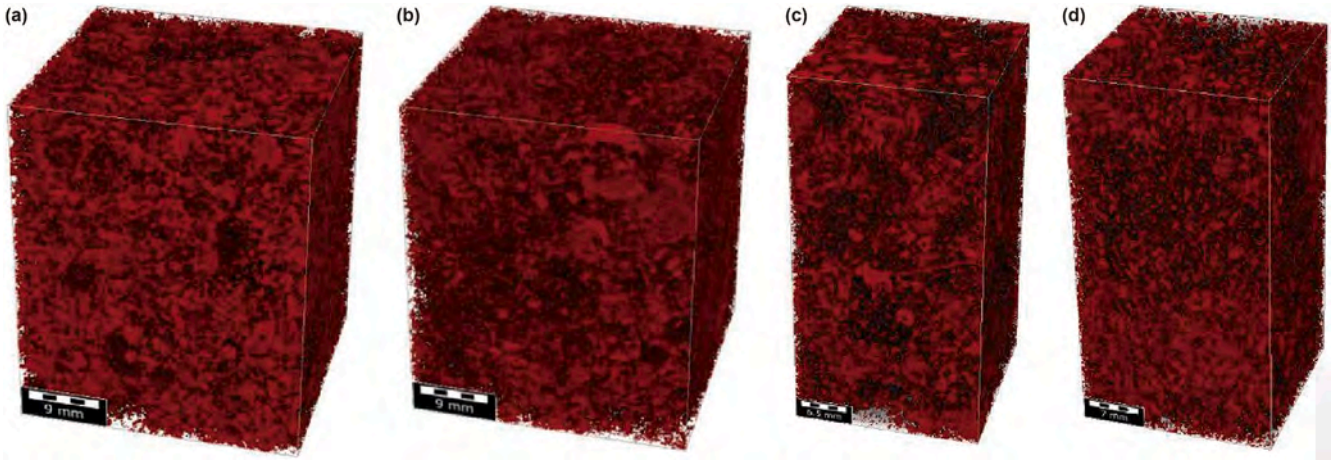

Fig. 10. Bulk pore distribution of the porous media (in red). Core plugs 2 (**a**) and 4 (**b**) (30 μm/voxel); miniatures 2 (**c**) and 4 (**d**) (20 μm/voxel).

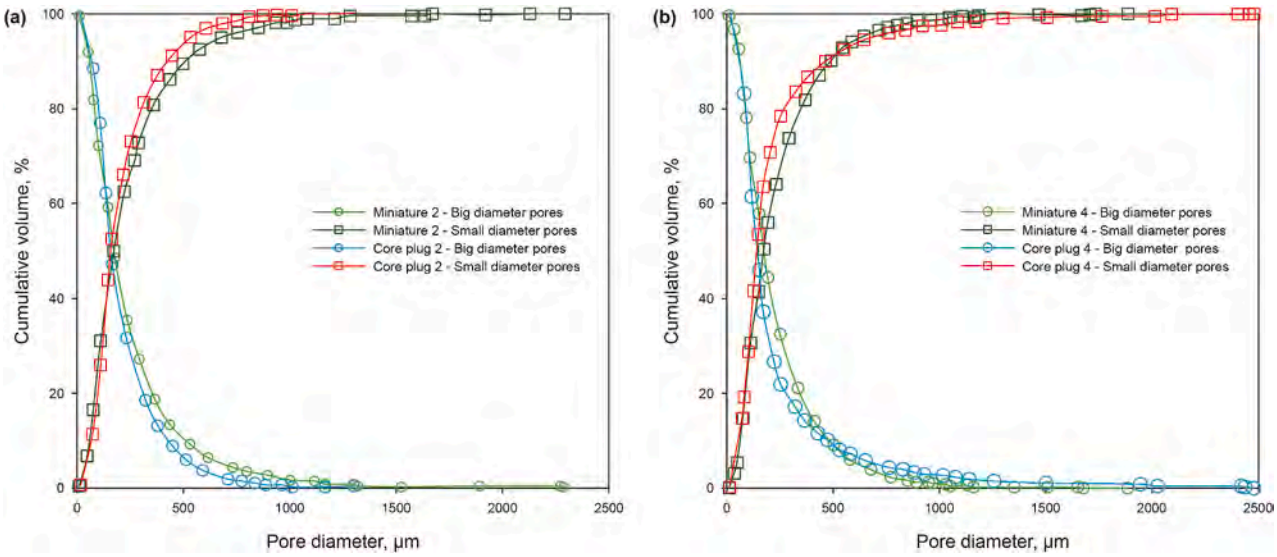

Fig. 11. Pore distribution of Core plugs 2 (**a**) and 4 (**b**) and their miniatures.

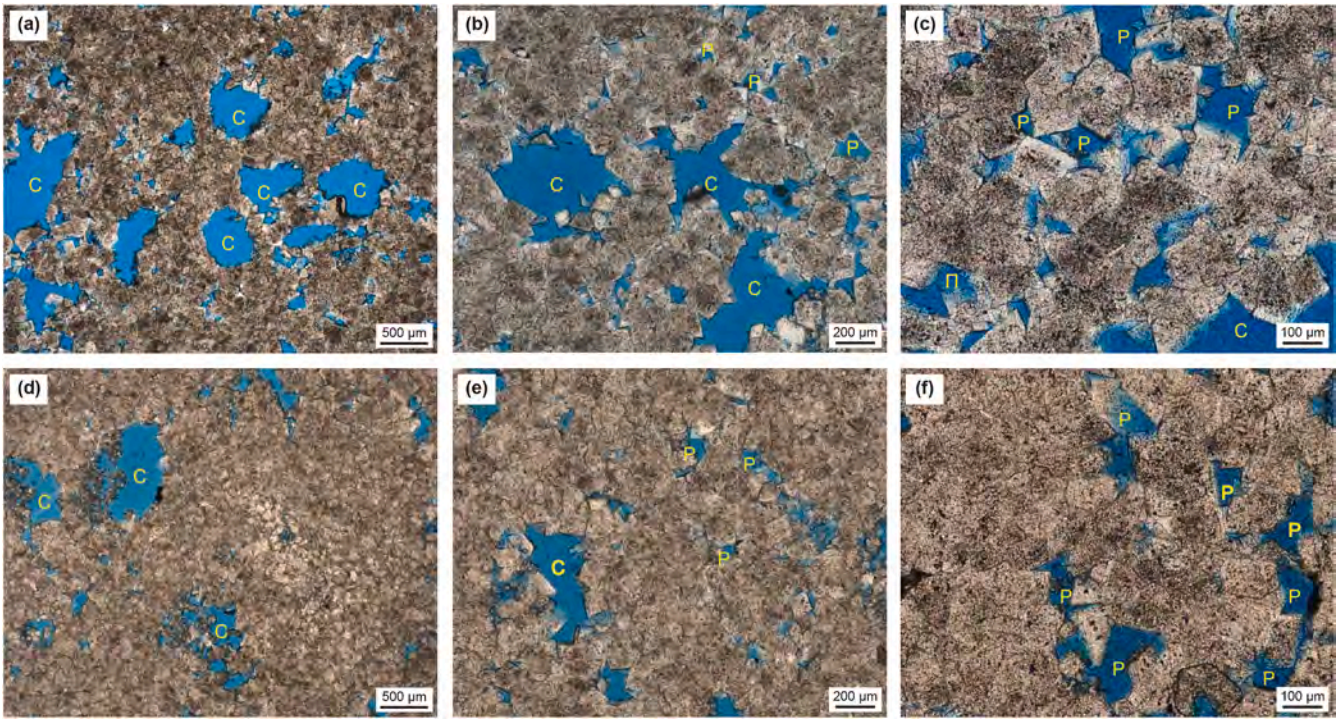

Fig. 12. Thin section images of crystalline dolostone samples. Samples 20 (**a**–**c**) and 18 (**c**–**f**) at different magnifications. Pore space includes cavities (C) and intercrystalline pores (P).

composition of the newly formed minerals closely matches that of dolomite (Ca, Mg, C, O), except for the absence of carbon. Carbon was likely removed from the system, potentially as a new compound, such as CO_2.

The microstructure and mineralogy of carbonate rocks subjected to thermal exposure have been previously studied by Karamov et al. (2022). In their work, the decomposition of dolomite resulted in the formation of oxides as complex micro- and nanostructures, along with traces of dolomite destruction.

The formation of anhydrite during thermal treatment was reported by Mukhametdinova et al. (2024) and Subbotina et al. (2023), and attributed to dolomite decomposition through intermediate stages involving $CaCO_3$ and CaO. Sulphur in this case was suggested to originate from fluids such as water or oil. Similarly, Mukhametdinova et al. (2023) described anhydrite formation, though in their study sulphur was derived from pyrite. In all cases, the primary source of calcium for anhydrite was carbonates, which decompose under thermal exposure.

The observed surface roughening and formation of technogenic minerals are consistent with recent studies of the thermal alteration of carbonate mineral matrices. However, the widespread formation of needle-shaped crystals composed of Ca, Mg, Si, and O

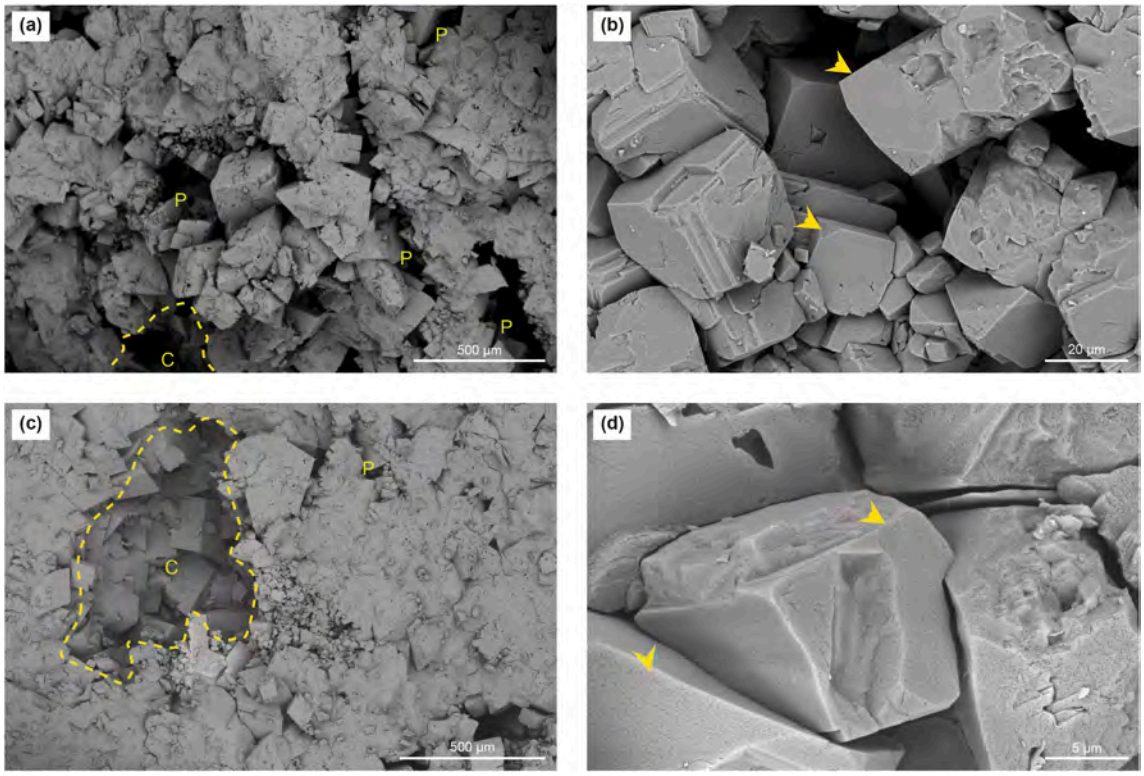

Fig. 13. SEM images of samples studied at the initial state. Samples 20 (**a**, **b**) and 18 (**c**, **d**) at different magnifications.

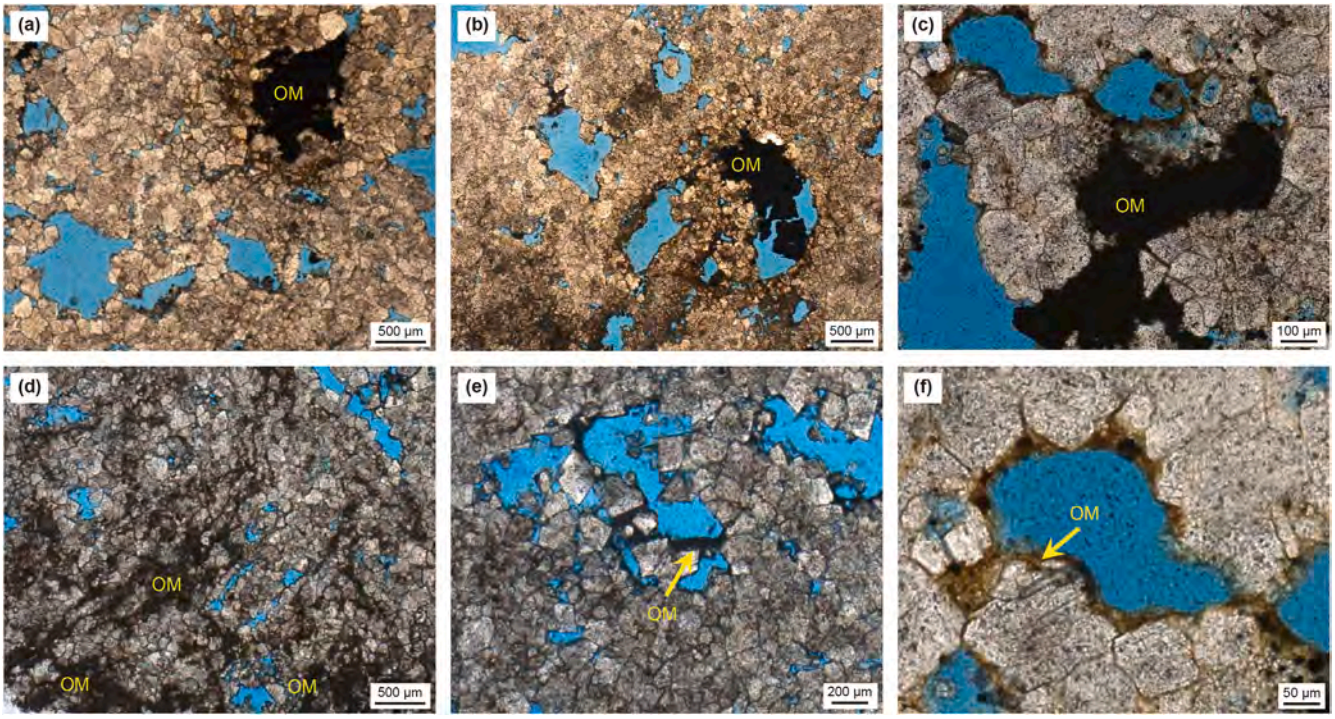

Fig. 14. Thin section images after the experiment. (**a**–**c**) Organic matter (OM) occupies cavities after the experiment (sample 19); (**d**) organic matter saturates the rock (sample 17); (**e**, **f**) organic matter forms thin films in the pores (sample 17).

appears to be a unique finding for dolomitic systems under ISC conditions. While similar acicular structures were recently identified as potential calcium hydrosilicates in heated limestones (Karamov et al., 2024; Tian et al., 2021), our EDX analysis confirms the critical role of magnesium derived from the host dolomite. The formation of these complex magnesium-calcium hydrosilicates,

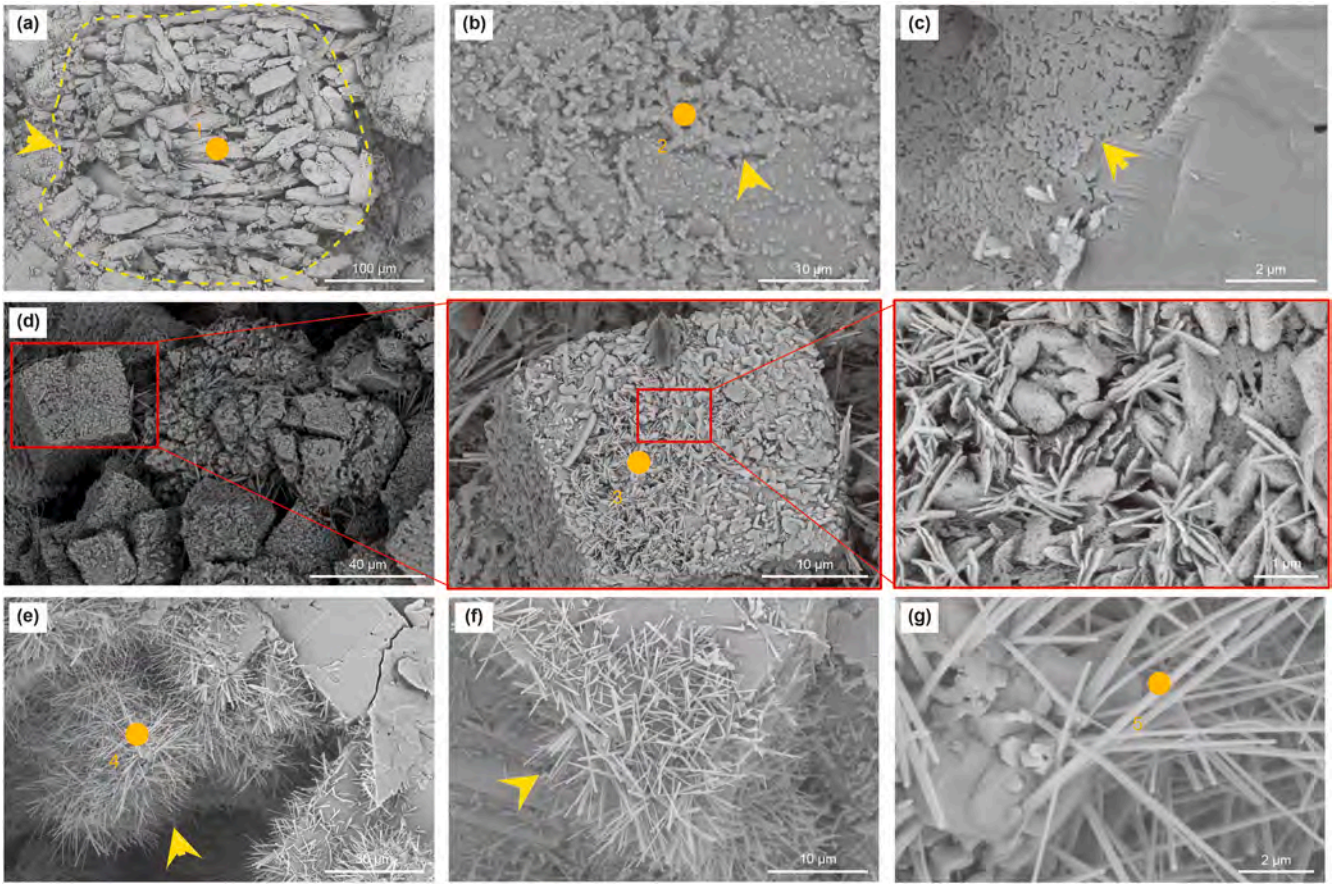

Fig. 15. SEM images illustrating key structural alterations observed. (**a**) Formation of anhydrite as inclusions consisting of separate elongated, oriented grains (sample 19); (**b**) formation of anhydrite aggregates filling pore spaces (sample 19); (**c**) evidence of dolomite edge destruction (sample 19); (**d**) complete transformation of a dolomite crystal into a nanocrystalline aggregate with needle-like and shapeless drip-like forms (sample 17); (**e**) widespread formation of needle crystal aggregates filling pore spaces (sample 17); (**f**, **g**) formation of needle-like crystals on the surface of dolomite crystals (sample 17). Yellow circles show the location at which samples were analyzed.

Table 5
Results of point analysis of elemental composition (EDX).

Point	Element mass, %					
	Oxygen	Magnesium	Calcium	Sulphur	Carbon	Silicon
1	37.80	4.56	31.71	23.71	2.23	–
2	49.55	10.05	24.84	11.51	4.05	–
3	56.63	13.69	26.88	2.80	–	–
4	51.02	11.89	6.53	–	–	30.57
5	44.29	5.18	37.35	–	1.72	11.47

which we observed to occlude up to 50% of the pore volume, represents a key mechanism for permeability damage that has not been previously incorporated into geochemical models of carbonate alteration during thermal EOR (Askarova et al., 2025).

In this work, we hypothesize that the observed needle-like crystals are magnesium-calcium hydrosilicate (CaH_2MgO_5Si) with a complex crystal structure. The experimental conditions, involving temperatures up to 700 °C, are consistent with reported formation temperatures for similar compounds (Karamov et al., 2022; Siauciunas et al., 2021). Additionally, their formation aligns with studies of the thermal treatment of carbonates (Lothenbach et al., 2015).

Further investigation using XRD analysis at higher concentrations is required to conclusively determine the specific mineralogical characteristics of the needle-like crystals. Nonetheless, their formation appears to complicate the pore structure by introducing new crystal growths while simultaneously occupying pore space due to dolomite decomposition.

3.4. Stable isotope analysis of C, H, N, S, and O using isotope ratio mass spectrometry (EA-IRMS)

The molecular and isotopic composition of gases generated during the experiment is presented in Tables 6 and 7. The total hydrocarbon gas content does not exceed 1.5%, with methane comprising 0.62% of the mixture. The molecular composition is dominated by nitrogen (up to 69%) and carbon dioxide (up to 28%), while hydrocarbon homologs from ethane to pentane are minute. This suggests high-temperature cracking of oil, as confirmed by the Bernard diagram (Fig. 16(a)) (Bernard et al., 1978). Furthermore, the co-existence of high concentrations of rock-derived CO_2 with H_2 generated from aquathermolysis could potentially facilitate secondary methanation or Fischer-Tropsch-type reactions, providing an additional pathway for methane formation alongside thermal cracking.

Methane shows $\delta^{13}C$ values ranging from −30.6‰ to −38.3‰ (PDB) and $\delta^{2}H$ values from −278‰ to −299‰ (VSMOW), indicating isotope fractionation with enrichment in the lighter carbon isotope, ^{12}C. These values are consistent with thermogenic origins (Fig. 16(b)) (He et al., 2019).

The $\delta^{2}H$ values of methane are significantly shifted to more negative “hydrothermal” values compared to gases formed during kerogen cracking. This shift may result from the presence of

Table 6
Gas molecular composition analysis captured during the experiment.

No.	Composition. %											
	He	H_2	O_2	N_2	CH_4	C_2H_6	C_3H_8	i-C_4H_{10}	n-C_4H_{10}	n-C_5H_{12}	CO_2	H_2S
1	1.48	0.10	0.10	66.43	0.62	0.29	0.39	0.06	0.08	0.06	28.82	0.05
2	1.70	0.07	0.10	69.37	0.41	0.21	0.34	0.05	0.07	0.05	25.48	0.05
3	23.98	0.08	0.17	3.37	0.24	0.12	0.13	0.03	0.04	0.03	19.83	0.02
4	30.68	0.10	0.11	49.27	0.28	0.12	0.11	0.02	0.03	0.02	17.53	–
5	23.53	0.07	0.11	49.79	0.18	0.09	0.10	0.02	0.03	0.03	24.24	0.01

Table 7
Carbon and hydrogen isotope composition of methane captured during the experiment.

Probe No.	$\delta^{13}C_{CH_4}$, ‰	$\delta^{2}H_{CH_4}$, ‰	$\delta^{13}C_{CO_2}$, ‰
1	–-30.6	−278.0	−3.1
2	−38.3	−291.0	−6.4
3	−35.6	−293.0	−2.1
4	−32.9	−288.0	−1.3
5	−36.5	−299.0	1.7

isotopically “light” hydrogen in water, which reacts with cracking products, thereby lowering the δ^2H of the resulting methane. A similar effect has been observed in oil cracking experiments, where pyrolysis under “dry” conditions produced methane with higher δ^2H values compared to pyrolysis conducted in the presence of isotopically light water (He et al., 2019).

However, the presence of water did not affect the δ^{13}C values of methane. Consistent with previous studies, the isotopic composition of methane in the combustion tube experiment shows a dependence on methane yield. At low methane concentrations, the δ^{13}C and δ^2H values are more negative, whereas higher methane concentrations result in heavier isotopic compositions. This trend reflects the isotopic characteristics of the initial oil and water (Fig. 17).

The CO_2 content in the gases produced during HTR ranges from 17.5% to 28.8%. The isotopic composition of carbon dioxide ($\delta^{13}C_{CO_2}$) varies from −6.4‰ to 1.7‰, closely matching the δ^{13}C of dolomite ($\delta^{13}C_{carb} \approx +3.2$‰, Table 8). This indicates that most of the CO_2 was generated through the thermal decomposition of carbonate material. At the same time, variations in $\delta^{13}C_{CO_2}$ values (−6.4‰ to 1.7‰) suggest the presence of CO_2 derived from the combustion of hydrocarbon cracking products.

Assuming the δ^{13}C of CO_2 from hydrocarbon combustion ranges from −38‰ (the most negative methane value, Table 9) to −29‰ (the most positive oil value), while the δ^{13}C of CO_2 from dolomite decomposition aligns with the δ^{13}C of dolomite (+3.2‰), the ratio of organic to mineral CO_2 in the gaseous products can be estimated using an isotopic balance equation. Calculations reveal that CO_2 from hydrocarbon combustion did not exceed 30% of the total CO_2. This finding underscores the paramount importance of accounting for gas source gas source (Zhou et al., 2021) and rock matrix reactions when interpreting produced gas composition during ISC in carbonates. While the contribution of carbonate decomposition to CO_2 generation is acknowledged in the literature, our isotopic analysis provides one of the first quantitative constraints for a dolomitic reservoir. This result challenges the assumptions used in some conventional combustion models, which may overestimate combustion efficiency if they attribute all produced CO_2 to hydrocarbon oxidation (Askarova et al., 2025; Meng et al., 2023). Accurate sourcing of CO_2 is therefore critical for both material balance calculations (Jiang et al., 2020) and for understanding the overall energy balance of the process.

The isotope analysis results of the rock samples are summarized in Table 8. Nitrogen and sulphur contents were below the detection limits of the analysis. The carbon and oxygen isotope compositions of the carbonates before the experiment remained unchanged after the combustion experiment, within the margin of

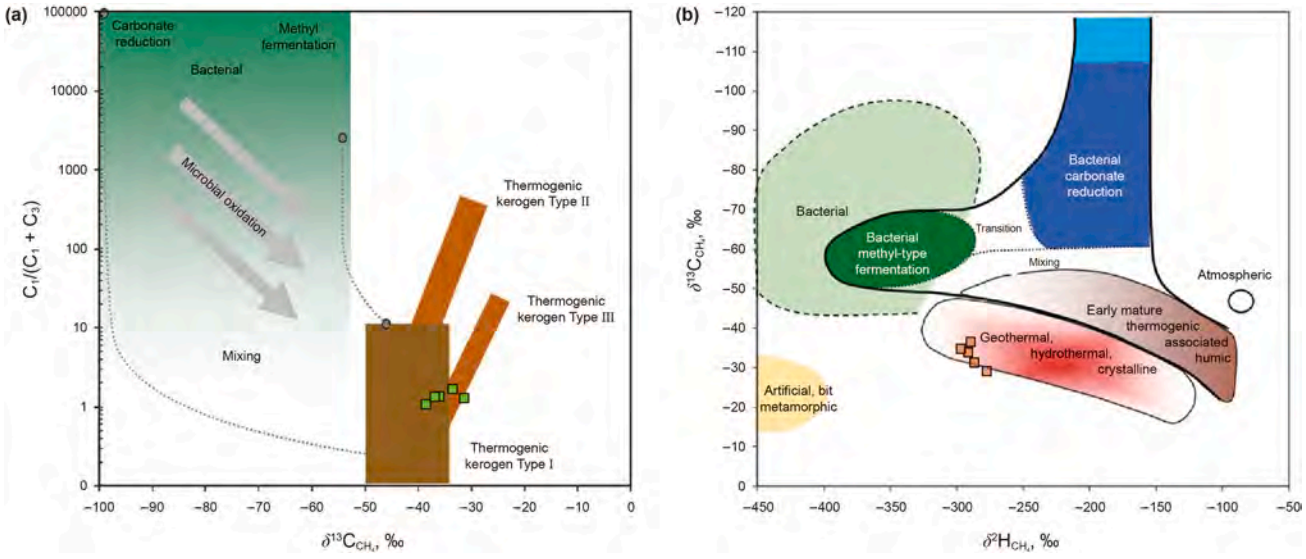

Fig. 16. Methane source classification diagrams based on isotopic data of carbon and hydrogen. (**a**) Bernard diagram indicates the thermogenic genesis of the methane; (**b**) a diagram for classifying bacterial and thermogenic natural gas using $\delta^{13}C_{CH_4}$–$\delta^{2}H_{CH_4}$ values.

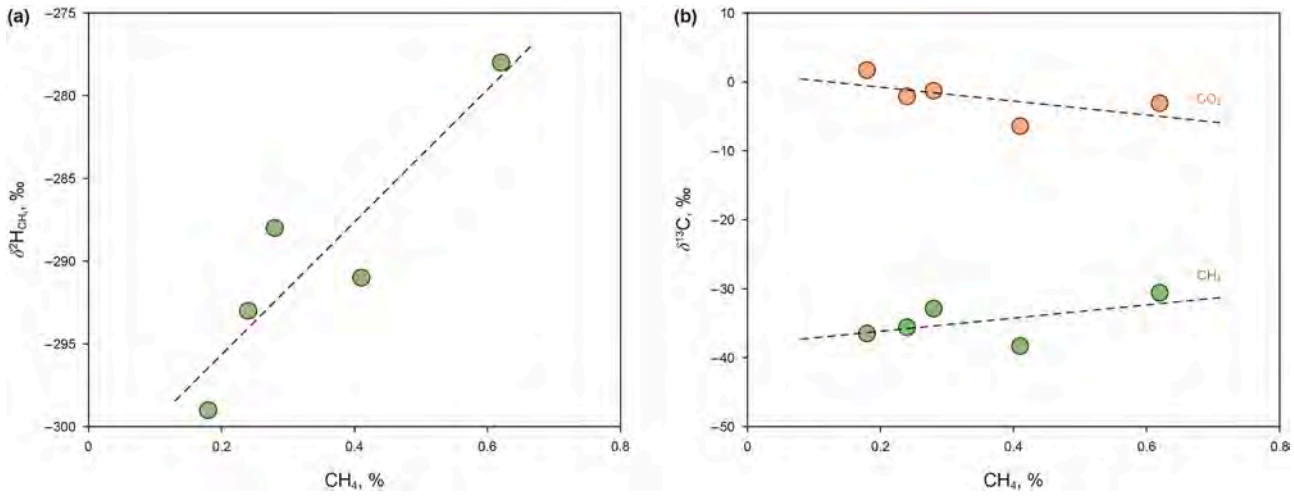

Fig. 17. Dependence of the hydrogen isotope composition of methane (**a**) and carbon isotope composition of CO_2 and methane on the methane content in the studied gases (**b**).

Table 8
Ilsotope composition of carbonate, organic carbon and oxygen, measured before and after the experiment.

Sample	$\delta^{13}C_{bulk}$, ‰	$\delta^{13}C_{carb}$, ‰	$\delta^{13}C_{org}$, ‰	$\delta^{18}O_{carb}$, ‰
Core inj	3.2	3.25	−21.8	−4.22
Core 12	2.9	3.12	−27.2	−4.64
Core 5	1.9	3.15	−25.4	−4.59
Core 3-1A	0.8	2.97	−25.4	−4.53
Core 2-3F	2.2	3.08	−27.4	−4.23

Table 9
Results of C, H, N, S elemental and isotope composition of oil during the experiment.

Sample	C, %	$\delta^{13}C$, ‰	H, %	$\delta^{2}H$, ‰	N, %	$\delta^{15}N$, ‰	S, %	$\delta^{34}S$, ‰
1 ini	89.0	−29.1	11.7	−92.7	0.59	4.6	2.6	9.1
2	86.7	−29.4	12.4	−91.6	0.57	5.0	2.4	8.9
3	87.9	−29.2	12.1	−89.1	0.44	4.7	2.4	9.2
4	87.7	−29.0	12.0	−92.7	0.42	5.4	2.3	9.2
5	87.6	−28.9	11.6	−93.2	0.39	5.6	2.0	8.9
6	85.3	−29.0	11.6	−91.4	0.37	6.0	2.3	9.3
7	84.8	−29.1	12.1	−91.6	0.33	5.6	2.0	9.3

measurement error. Initially, the organic carbon content in the original rock was extremely low (fractions of a percent) but tripled during the experiment, likely due to the deposition of incomplete combustion products, such as coke. This increase in carbon content was accompanied by a decrease in $\delta^{13}C$ values from −21.8‰ to −27.4‰, suggesting a genetic link between the deposited carbon and the experimental oil (Table 8).

No significant isotopic shifts were observed in sulphur ($\delta^{34}S \approx 9$‰) or hydrogen fractions of the oil (Table 9), indicating that variations remain within analytical precision. However, nitrogen content in the oil was halved, with $\delta^{15}N$ values increasing from 4.6‰ to 6‰, reflecting the destruction and removal of nitrogen-bearing compounds as gaseous products during thermal and oxidative processes (Fig. 18).

3.5. Permeability and porosity measurement

Lack of information about the altered reservoir rock properties after the ISC recovery technique is the motivation to conduct permeability and porosity assessment at the laboratory conditions. The improvement in rock properties of limestones after its disassociation at high temperatures was noticed by Marchant and Menzie (1966).

The results of the permeability and porosity measurements of untouched core plug miniatures are presented in Fig. 19. As was discussed earlier, the values obtained via the micro-CT might display slightly lower porosity than those obtained from the porosimeter. For instance, Miniature 2 displayed a porosity of 10.75% and 13.39% from the micro-CT scanner and porosimeter, respectively.

To mimic the thermal decomposition of the core plugs that occurred during the combustion tube test, the miniatures were pre-weighed and placed in the oven and were incrementally heated at 150, 300, 450, and 650 °C at atmospheric pressure for 4 h. Throughout the core decomposition test, there was no source of the continuous gas (air) injection, however, the air entered the oven every time, when the samples were taken out for weighing. The temperature of 650 °C was used as it was close to the corresponding maximum combustion tube temperature, at which a mass loss equivalent to the combustion tube test was expected to occur. Two miniatures were later used to create a vug proportionally to the ones used in the CT experiment and were referred to as “Vuggy core” with a vug volume of 3 cm^3 (vs. 8 cm^3 in the bigger versions that were used for the combustion tube). To evaluate the effect of chlorite salts on the core decomposition, Core plug 3 was pressure vacuumed, air flooded, evacuated under vacuum again, and brine saturated at 5000 psig before being placed in the oven. The results of the mass losses of different samples are presented in Fig. 21.

No evidence of enhanced core decomposition has been noticed for the sample initially saturated by brine. The color difference of the three core plugs named “Whole”, “Brine saturated”, and “Vuggy” exposed to different temperatures can be observed in the photograph presented in Fig. 20. It should be noted that the original color of the samples was close to the color of Brine saturated core. The white precipitates or salt on the Brine saturated core were a result of the water evaporation.

The mass loss was almost independent of the temperature rise to 450 °C (see Fig. 14). At 650 °C the mass loss reached 23% for the mechanically untouched samples and 13% for the vug-induced core plug. The mass loss of 23% is aligned with the finding reported by Olszak-Humienik and Jablonski (2015).

By comparing the mass loss of the core plugs that were extracted from the combustion tube versus their miniatures, the

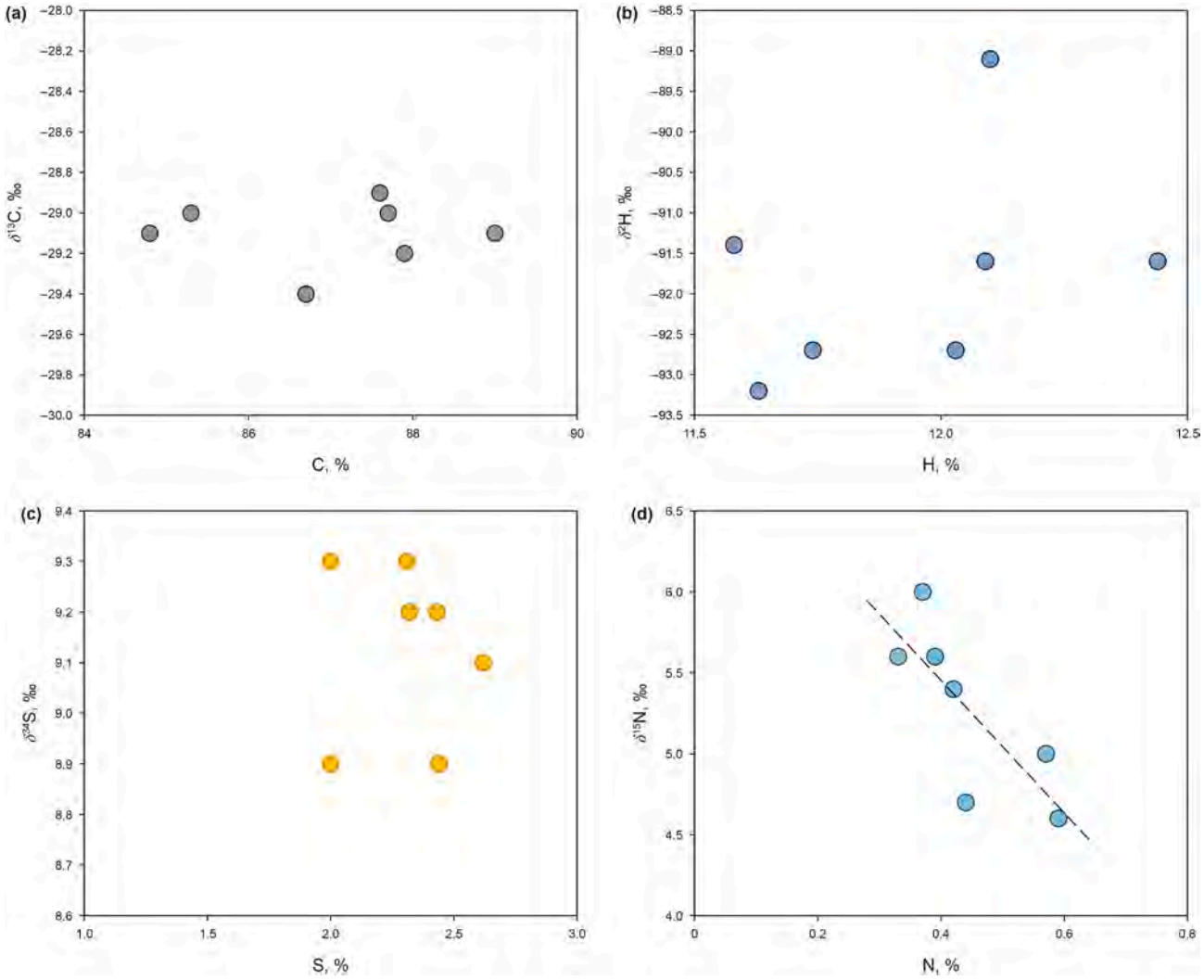

Fig. 18. Dependence of isotope and elemental composition. (**a**–**c**) shows no significant correlations; (**d**) nitrogen isotopic composition becomes heavier with decreasing nitrogen content.

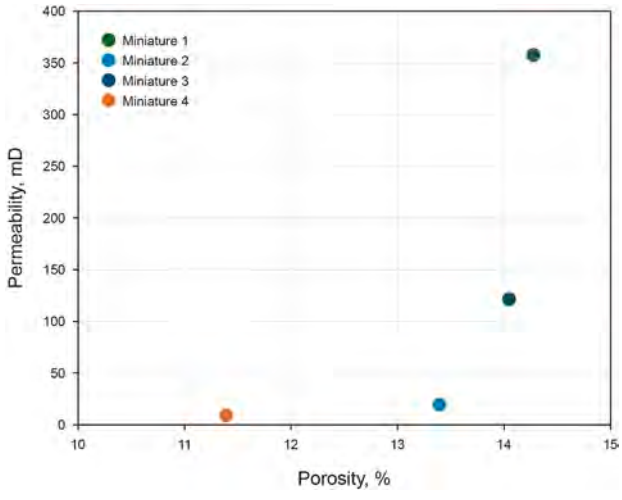

Fig. 19. Original permeability and porosity of miniature core plugs.

mass loss that occurred in the big core plugs was significantly less (around 4%) (Fig. 21). By interpolation (Fig. 21), the actual temperature that the core plugs experienced during the ISC test can be found, which corresponds to about 480–490 °C.

The porosimetry measured reservoir rock properties before and after the heating are shown in Fig. 22, where 2 out of 3 samples showed an improvement in the permeability values. The black marks represent the original values, while the red marks are the values after heat exposure.

To increase the statistical sample size and develop an understanding of the permeability change with the dolomite decomposition, an additional five core plugs (Core plugs A–E), sampled from the same outcrop as the big core plugs, were tested. As a drastic mass change was observed at the temperature of 650 °C after 4 h of heating, the rest of the samples underwent isothermal heating at 650 °C for 4 h as well. Like the previous experiments, the permeability and porosity were measured before and after the core decomposition test, and the results are presented in Fig. 23. The mass loss (before and after the core decomposition tests) varied between 21% and 23% from the initial sample weights. For the consistency of

Fig. 20. Photographs of Whole, Vuggy, and Brine saturated cores.

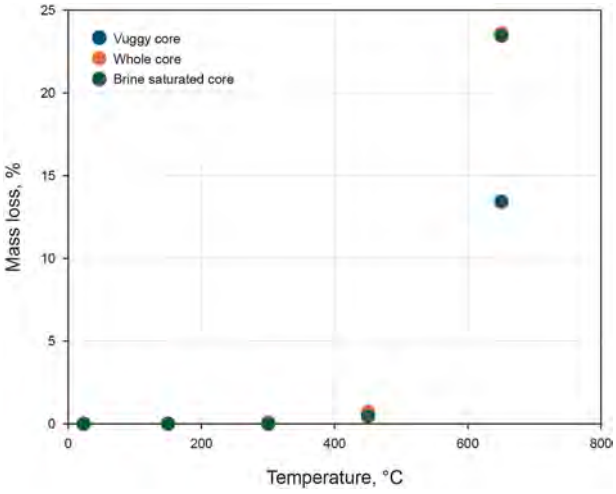

Fig. 21. Mass loss of Whole, Vuggy, and Brine saturated cores.

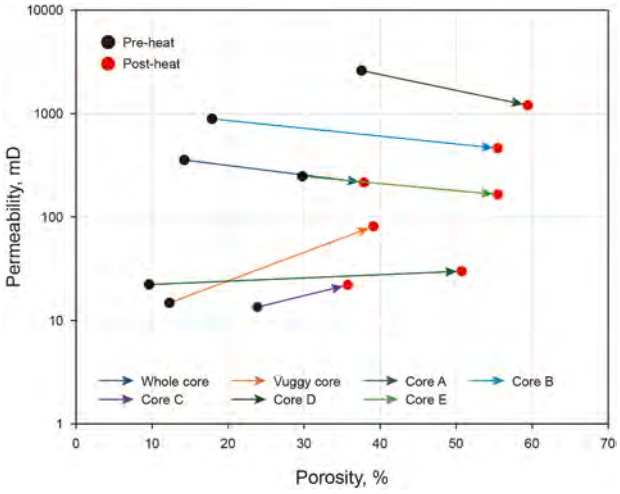

Fig. 23. Permeability and porosity of miniature cores.

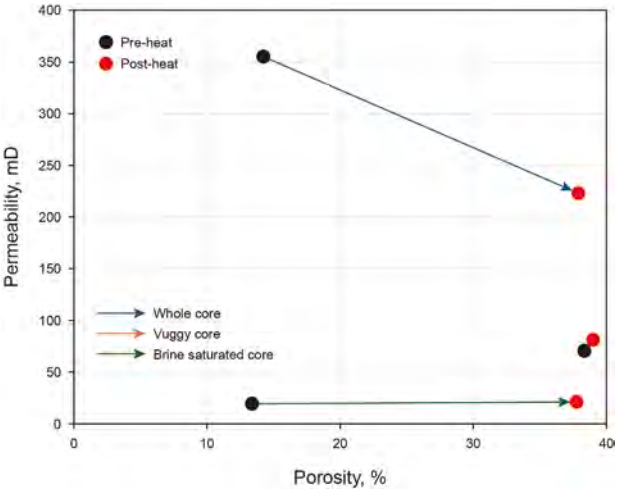

Fig. 22. Permeability and porosity of Whole, Vuggy, and Brine saturated cores.

the compared samples, the Vuggy core plug was excluded from further core evaluation. The black marks represent the original values, while the red marks are the values after heat exposure.

Having analyzed the tendency of the permeability change, it was found that four of the seven samples demonstrated a decrease in permeability. However, this observation was relevant to the samples, in which original permeability varied between 247 and 2600 mD, or in other words for relatively highly permeable samples. To achieve stable permeability values each test was repeated at least 5 times. Every cycle, when helium passed through the core body, the permeability increased (Fig. 24). This approach was fundamental not only to obtain consistency in the measured values but also to imitate a similar case in the field where air injection is a continuous process. Hence, the permeability increase could be justified by the fine migration within the matrix, where the decomposed particles get rearranged with the gas stream.

In the case of the low-permeable (13–247 mD) core plugs, the permeability values improved from between 24% to more than 500% depending on the sample.

To try to understand why certain samples demonstrated an increase in permeability values, while other core plugs deteriorated, the correlation between porosity and permeability was considered in relationship to the rock fabric number (λ), an aspect that likely has not been considered previously in the in-situ combustion literature. Rock fabric, in geological terms, refers to the characterization of the pore space within a rock, considering the impact of particle size and sorting on the interrelationship

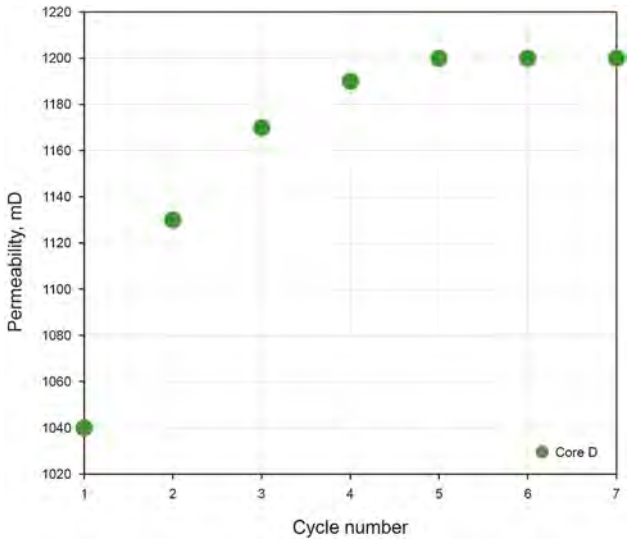

Fig. 24. Permeability measurements of Core D.

between porosity and permeability. When λ ranges between 0.5 and 1.5 the carbonate is generally considered to be a grainstone; when λ ranges between 1.5 and 2.5 the carbonate is generally a packstone; when λ ranges between 2.5 and 4.0 the carbonate is generally a wackstone (Fig. 25). The concept of rock fabric number was developed by Jennings and Lucia (2003).

The paradoxical permeability inversion is explained by a competition between two mechanisms, with the outcome dictated by the initial rock fabric:

(1) Pore-throat pugging in grainstones: In high-permeability grainstones, flow occurs through large, well-connected pores. These open spaces facilitate the extensive growth of neoformed, needle-shaped magnesium-calcium hydrosilicate crystals, as observed in our SEM analysis. These crystals physically obstruct large pore throats, causing a catastrophic reduction in permeability.

(2) Induced microfracturing in packstones/wackstones: In low-permeability, matrix-supported rocks, flow is initially restricted to tortuous micropores. The decomposition of dolomite throughout the matrix causes significant solid mass loss (up to 23%) and vigorous internal CO_2 gas generation. This process induces a network of new microfractures that act as new, high-conductivity flow paths, bypassing the original poor pore system. The net effect is a marked improvement in bulk permeability, as the benefit of new fractures outweighs any plugging of the already inefficient micropores.

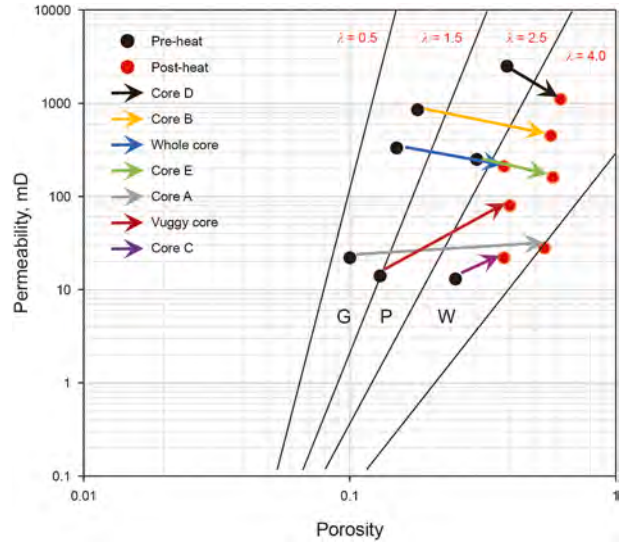

Fig. 25. Rock-fabric number, permeability, and porosity of the core plugs; λ between 0.5 and 1.5 corresponds to grainstone (G) carbonate; λ between 1.5 and 2.5 corresponds to packstone (P), and λ between 2.5 and 4.0 corresponds to wackstone (W). Rock fabric lines after Jennings and Lucia (2003).

While previous experimental studies of thermal EOR in carbonates have reported permeability alterations (Mogensen and Masalmeh, 2020; Mohammadi and Mahmoudi Alemi, 2023; Mukhametdinova et al., 2023), the results have often appeared contradictory, with both damage and stimulation being observed. Our hypothesis is that these conflicting observations can be reconciled by considering the initial rock fabric, an aspect largely overlooked in prior ISC literature. By classifying our samples into grainstones, packstones, and wackstones, we can systematically analyze how the same thermal process leads to divergent permeability responses. This approach moves beyond a simple porosity–permeability relationship and provides a more robust framework for predicting reservoir quality evolution, a critical need for improving the reliability of numerical reservoir simulations (Askarova et al., 2025; Meng et al., 2023).

Another point of interest has to do with the change in pore throat (port) size between pre- and post-heat conditions. The port subject has been summarized by Hartmann and Beaumont (1999) in the AAPG literature and has been demonstrated with different types of rocks including carbonates by Aguilera (2014).

Hartmann and Beaumont (1999) indicate that analyzing permeability and porosity data separately to characterize rock quality can be deceiving. It is more effective to work with the ratio of permeability and porosity for determining rock quality or to go beyond it for estimating the pore throat aperture of the rocks. This is done in Fig. 26, where r_{p35} is the radius of the pore throat aperture at 35% cumulative pore volume. This type of graph is generally referred to as a flow units plot.

Dale Winland, an Amoco researcher, found that the effective pore system that dominates flow through a rock generally corresponds to a mercury saturation of 35% during a capillary pressure test (Winland, 1972). Fig. 25 includes the same pre- and post-heat porosities and permeabilities presented in Figs. 22 and 24. The crossplot shows megaports (r_{p35} > 10 μm), macroports (2 to 10 μm), mesoports (0.5 to 2 μm), and microports (0.1 to 0.5 μm).

The three upper samples (black dots) fall within the megaport region with large pore throat radii. at original preheating conditions. Following in-situ combustion the samples (red dots) show significant reductions in permeability and pore throat aperture. Samples with pre-heat permeabilities below 100 mD show some post-heat increase; however, their pore throat radii remain approximately the same in the lower part of the macroport region.

The conclusion is reached that the reduction in post-heat port throat radii illustrated by the red dots is consistent with the rock fabric number discussed above which shows a reduction in the quality of the rocks. These findings might prove of value in future combustion tests and reservoir simulation studies.

Flow unit description shown in Fig. 26 shows that three pre-heat cores (black dots) fall in the region dominated by megaports, one sample in the upper macroport region and three samples in the lower macroport region. Thus, all the samples have

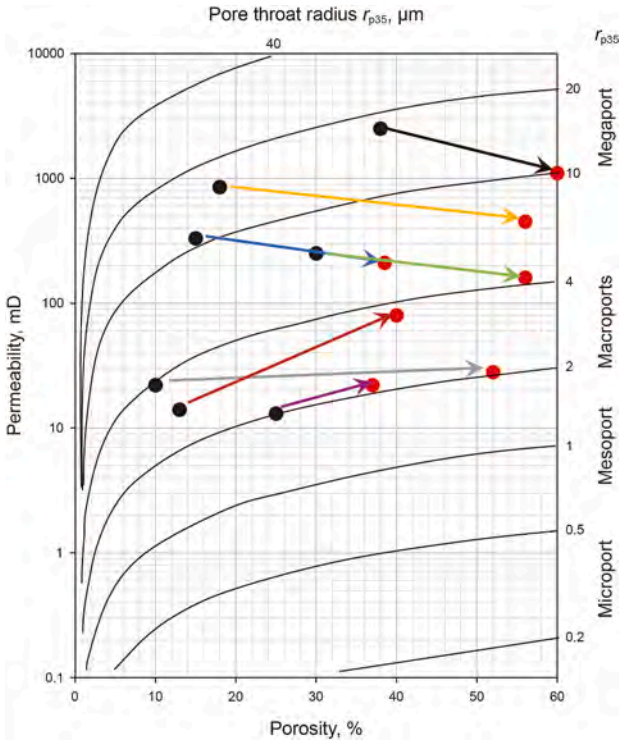

Fig. 26. Pore throat radii, permeability, and porosity for the pre- and post-heat core plugs, r_{p35} lines after Aguilera (2014).

important radii at original conditions. Following in-situ combustion the samples (red dots) show important reductions in permeability. Samples with pre-heat permeabilities below 100 mD show some post-heat increase; however, their pore throat radii remain approximately the same in the lower part of the macroport region.

It should be noted that the experiments described above differ from actual in-situ ISC conditions as they were done at atmospheric pressure, without oil or brine saturation, and did not undergo a combustion process. Hence, it is recommended to evaluate these experiments keeping into account all the nuances to evaluate the adequacy of the obtained findings.

4. Conclusions

This multi-scale, post-combustion analysis of a vuggy dolomite reservoir reveals that in-situ combustion (ISC) induces a fundamental and paradoxical permeability inversion. The primary quantitative finding is that initially high-permeability samples (up to 2600 mD) experienced significant permeability damage, while initially low-permeability samples (<250 mD) showed marked improvement. This was accompanied by a significant reduction in pore throat radii, with the flow regime shifting from a megaport-dominated to a macroport-dominated system.

The mechanism driving this inversion is the thermal decomposition of the rock matrix at temperatures of 480–490 °C, leading to a significant mass loss of the rock (up to 23%). This process fundamentally altered the rock fabric, transforming it from a high-quality grainstone/packstone (rock-fabric number, $\lambda \approx 1.5$–2.5) to a low-quality wackstone-like character ($\lambda \approx 4.0$).

Micro-scale analysis provided direct evidence for this mechanism. The neoformation of pore-occluding, needle-shaped magnesium-calcium hydrosilicate crystals was observed, occupying up to 50% of the pore space in high-quality rock. The dominance of this mineralogical reaction over oil burning was confirmed by stable isotope analysis, which quantified that up to 70% of the produced CO_2 originated from dolomite decomposition, with only 30% derived from hydrocarbon combustion.

The implications of these findings are critical for the planning and monitoring of ISC projects in carbonate reservoirs. First, initial permeability and porosity alone are poor predictors of post-combustion reservoir quality; the geochemical reactivity and thermal stability of the rock fabric are paramount. The rock-fabric number (λ) may serve as a more robust metric for predicting a reservoir's response to thermal stress. Second, produced gas analysis must account for the significant contribution of mineral-derived CO_2 to accurately assess combustion front efficiency and stoichiometry.

Ultimately, this work provides a rock-based, mechanistic framework for understanding reservoir alteration during ISC, but further research is needed. Future experimental work should investigate the impact of confining pressure and brine chemistry on these mineralogical transformations. A critical parallel challenge is the upscaling of these core-scale findings for reservoir simulation. Predictive models must evolve to incorporate rock-fabric-dependent alterations, including dynamic changes in relative permeability, geomechanical properties, and potentially transitioning to dual-porosity frameworks to account for induced microfracturing. Integrating these complex mechanisms is paramount for refining predictive models and accurately forecasting ISC performance in heterogeneous carbonate systems.

CRediT authorship contribution statement

Rita Fazlyeva: Writing – review & editing, Writing – original draft, Visualization, Investigation, Formal analysis, Data curation, Conceptualization. **Tagir Karamov:** Writing – review & editing, Writing – original draft, Visualization, Methodology, Investigation. **Matthew Ursenbach:** Supervision, Methodology, Conceptualization. **Roberto Aguilera:** Validation, Resources, Project administration, Formal analysis. **Andrey Voropaev:** Methodology, Investigation. **Mikhail Spasennykh:** Writing – review & editing, Supervision, Resources, Project administration, Funding acquisition, Formal analysis. **Gordon Moore:** Writing – review & editing, Supervision, Resources. **Alexey Cheremisin:** Resources, Project administration. **Mehta Sudarshan:** Writing – review & editing, Supervision, Project administration, Methodology, Investigation, Conceptualization.

Declaration of competing interest

The authors declare that they have no known competing financial interests or personal relationships that could have appeared to influence the work reported in this paper.

References

Aguilera, R., 2014. Flow units: From conventional to tight gas to shale gas to tight oil to shale oil reservoirs. In: SPE Reservoir Eval. Eng. https://doi.org/10.2118/165360-PA.

Akbar, M., Vissapragada, B., Alghamdi, A.H., Allen, D., Herron, M., Carnegie, A., Dutta, D., Olesen, J.-R., Chourasiya, R.D., Logan, D., Stief, D., Netherwood, R., Russell, S.D., Saxena, K., 2000. A snapshot of carbonate reservoir evaluation. Oilfield Rev. 12, 20–41.

Alizadeh, A., 2020. A Robust Kinetic Model for Computer Modelling of In Situ Combustion Processes in Athabasca Oil Sands. Doctoral Dissertation. University of Calgary, Alberta, Canada.

Antolinez, J.D., Miri, R., Nouri, A., 2023. In situ combustion: A comprehensive review of the current state of knowledge. Energies 16 (17). https://doi.org/10.3390/en16176306.

Askarova, A., Alekhina, T., Fazlyeva, R., Popov, E., Mehta, S.R., Moore, R.G., Ursenbach, M.G., Cheremisin, A., 2025. In situ combustion performance in heavy

oil carbonate reservoirs: A triple-porosity numerical model. Appl. Therm. Eng. 258, 124535. https://doi.org/10.1016/j.applthermaleng.2024.124535.
Baudin, F., Bouton, N., Wattripont, A., Carrier, X., 2023. Carbonates thermal decomposition kinetics and their implications in using Rock-Eval® analysis for carbonates identification and quantification. Sci. Technol. Energy Trans. 78. https://doi.org/10.2516/stet/2023038.
Bennion, D.W., Donnelly, J.K., Moore, R.G., 1977. Effects of the fireflooding temperature on mineral composition and bitumen properties. Canadian Institute of Mining and Metallurgy. In: Canada-Venezuela Oil Sands Symposium. Edmonton.
Bernard, B.B., Brooks, J.M., Sackett, W.M., 1978. Light hydrocarbons in recent Texas continental shelf and slope sediments. J. Geophys. Res. Oceans 83 (C8), 4053–4061.
Buxton, T.S., Pollock, C.B., 1974. The Sloss COFCAW project-further evaluation of performance during and after air injection. J. Pet Technol. 26 (12), 1439–1448. https://doi.org/10.2118/4766-PA.
Caceres, P.G., Attiogbe, E.K., 1997. Thermal decomposition of dolomite and the extraction of its constituents. Miner. Eng. 10, 1165–1176. https://doi.org/10.1016/S0892-6875(97)00101-5.
Dunham, R.J., Ham, W.E., 1962. Classification of carbonate rocks according to depositional texture1. In: Classification of Carbonate Rocks—A Symposium. American Association of Petroleum Geologists.
Erdman, N., Drenzek, N., 2013. Integrated preparation and imaging techniques for the microstructural and geochemical characterization of shale by scanning electron microscopy. Electron Microscopy of Shale Hydrocarbon Reservoirs. Camp, W., Diaz, E., and Wawak, B., AAPG Memoir.
Fatemi, S.M., 2009. Investigation of top-down in-situ combustion process in complex fractured carbonate models: Effects of fractures' geometrical properties. In: SPE Canada Unconventional Resources Conference. https://doi.org/10.2118/149314-MS.
Fazlyeva, R., Ursenbach, M., Mallory, D., Mehta, S., Cheremisin, A., Moore, G., Spasennykh, M., 2023. In situ combustion of heavy oil within a vuggy carbonate reservoir: Part I—Feasibility study. Energies 16, 2233. https://doi.org/10.3390/en16052233.
Hartmann, D.J., Beaumont, E.A., 1999. Predicting reservoir system quality and performance. In: Beaumont, E.A., Foster, N.H. (Eds.), Exploring for Oil and Gas Traps. AAPG Treatise of Petroleum Geology, Handbook of Petroleum Geology, pp. 9–154.
Hascakir, B., Kovscek, A.R., 2014. Analysis of in-situ combustion performance in heterogeneous media. In: SPE Heavy Oil Conference-Canada. https://doi.org/10.2118/170008-MS.
He, K., Zhang, S., Mi, J., Fang, Y., Zhang, W., 2019. Carbon and hydrogen isotope fractionation for methane from non-isothermal pyrolysis of oil in anhydrous and hydrothermal conditions. Energy Explor. Exploit. 37 (5), 1558–1576.
Hogue, B., Gutierrez, D., Hong, C., Steiner, J., Freeman, L., 2015. Oil recovery from gas-over-bitumen reservoirs: Results from the AIDROH Pilot Project in Alberta. J. Can. Pet. Technol. 54 (6), 351–360. https://doi.org/10.2118/174455-PA.
Jennings, J.W., Lucia, F.J., 2003. Predicting permeability from well logs in carbonates with a link to geology for interwell permeability mapping. SPE Reservoir Eval. Eng. 6 (4), 215–225. https://doi.org/10.2118/84942-PA.
Jha, K.N., Verkoczy, B., 1986. The role of thermal analysis techniques in the in-situ combustion process. SPE Reserv. Eng. 1 (4), 329–340. https://doi.org/10.2118/12677-PA.
Jiang, H., Yuan, S., Li, L., Wang, J., Wang, H., Li, T., 2020. Operation control of in situ combustion based on the material balance equation. J. Can. Pet. Technol. (1), 8898054. https://doi.org/10.1155/2020/8898054.
Karamov, T., White, V., Idrisova, E., Kozlova, E., Burukhin, A., Morkovkin, A. Spasennykh, 2022. Alterations of carbonate mineral matrix and kerogen microstructure in domanik organic-rich shale during anhydrous pyrolysis. Minerals 12 (7), 870. https://doi.org/10.3390/min12070870.
Karamov, T.I., Popov, E. Yu, Khairullina, A.I., Spasennykh, M. Yu, Lesina, N.V., Prokhorova, A.A., Bakumenko, E.A., Protsenko, A.N., Ryazanov, A.A., Ermakov, A.S., 2024. Technology-induced mineral formation in carbonate rocks-reservoirs of heavy hydrocarbons under laboratory high-temperature filtration experiments. OIJ (1), 60–64. Paper Number: OIJ-2024-01-060-064-RU. (in Russia).
Krivovichev, S.V., Shcherbakova, E.P., Nishanbaev, T.P., 2010. The crystal structure of $CaMg_2(SO_4)_3$, a mineral phase from coal dumps of the Chelyabinsk Coal Basin, Russia. Can. Mineral. 48, 1469–1475. https://doi.org/10.3749/canmin.48.5.1469.
Li, M., Messing, G., 1983. Chloride salt effects on the decomposition of dolomite. Thermochim. Acta 68 (1), 1–8. https://doi.org/10.1016/0040-6031(83)80373-6.
Lothenbach, B., Nied, D., L'Hôpital, E., Achiedo, G., Dauzères, A., 2015. Magnesium and calcium silicate hydrates. Cement Concr. Res. 77, 60–68. https://doi.org/10.1016/j.cemconres.2015.06.007.
Marchant, L.C., Menzie, D.E., 1966. Limestone rock changes by in-situ combustion temperatures. Prod. Mon. 30 (11).
Mazzullo, S.J., 2004. Overview of porosity evolution in carbonate reservoirs. Kansas Geol. Soc. Bull. 79 (1–2), 1–19. http://www.searchanddiscovery.com/documents/2004/mazzullo/ (accessed 7.17.19).
McIntosh, R., Sharp, J., Wilburn, W., 1990. The thermal decomposition of dolomite. Thermochim. Acta 165 (2), 281–296. https://doi.org/10.1016/0040-6031(90)80228-Q.
Meng, F., Wang, Y., Song, X., Hao, M., Qin, G., Qi, Y., Ma, Z., Wang, D., 2023. Numerical simulation of fracture flow interaction based on discrete fracture model. Processes 11 (10). https://doi.org/10.3390/pr11103013.
Miller, R., 1995. Koch's experience with deep in situ combustion in Williston basin. Presented at the Field Application in Situ Combustion Practices: Past, Present and Future Applications, Tulsa, OK (United States), 21-22 Apr 1994.
Mogensen, K., Masalmeh, S., 2020. A review of EOR techniques for carbonate reservoirs in challenging geological settings. J. Pet. Sci. Eng. 195. https://doi.org/10.1016/j.petrol.2020.107889.
Mohammadi, S., Mahmoudi Alemi, F., 2023. Permeability impairment and oil recovery changes in porous media due to asphaltenes deposition during natural gas injection: An experimental study. Fuel Commun. 17, 100096. https://doi.org/10.1016/j.jfueco.2023.100096.
Moore, R.G., Belgrave, J.D.M., Mehta, R., Ursenbach, M., Laureshen, C.J., Xi, K., 1992. Some insights into the low-temperature and high-temperature in-situ combustion kinetics. In: SPE Improved Oil Recovery Conference. https://doi.org/10.2118/24174-MS.
Mukhametdinova, A., Karamov, T., Popov, E., Burukhin, A., Kozlova, E., Usachev, G., Cheremisin, A., 2023. Reservoir properties alteration in carbonate rocks after in-situ combustion. SPE Reservoir Eval. Eng. 26 (2), 330–347. https://doi.org/10.2118/212281-PA.
Mukhametdinova, A., Karamov, T., Markovic, S., Morkovkin, A., Burukhin, A., Popov, E., Sun, Z.-Q., Zhao, R., Cheremisin, A., 2024. Exploring in-situ combustion effects on reservoir properties of heavy oil carbonate reservoir. Pet. Sci. 21 (5), 3363–3378. https://doi.org/10.1016/j.petsci.2024.04.014.
Okere, C.J., Sheng, J.J., 2023. Review on clean hydrogen generation from petroleum reservoirs: Fundamentals, mechanisms, and field applications. Int. J. Hydrogen Energy 48 (97), 38188–38222. https://doi.org/10.1016/j.ijhydene.2023.06.135.
Okere, C.J., Sheng, J.J., 2024. A new modelling approach for in-situ hydrogen production from heavy oil reservoirs: Sensitivity analysis and process mechanisms. Energy 302. https://doi.org/10.1016/j.energy.2024.131817.
Okere, C.J., Sheng, J.J., 2025. Optimizing hydrogen generation from petroleum reservoirs: A dual-perspective approach for enhancing efficiency and cleaner production. Gas Sci. Eng. 136. https://doi.org/10.1016/j.jgsce.2025.205576.
Olszak-Humienik, M., Jablonski, M., 2015. Thermal behavior of natural dolomite. J. Therm. Anal. Calorim. 119, 2239–2248. https://doi.org/10.1007/s10973-014-4301-6.
Perry, C., Gillot, J., 1982. Mineralogical transformations as indicators of combustion zone temperatures during in situ combustion. Bull. Can. Pet. Geol. 30 (1), 34–42. https://doi.org/10.35767/gscpgbull.30.1.034.
Pope, C., Ismail, N.B., Hascakir, B., 2020. Catalytic impact of clays during in-situ combustion. In: SPE Improved Oil Recovery Conference. https://doi.org/10.2118/200381-MS.
Seidy-Esfahlan, M., Tabatabaei-Nezhad, S.A., Khodapanah, E., 2024. Comprehensive review of enhanced oil recovery strategies for heavy oil and bitumen reservoirs in various countries: Global perspectives, challenges, and solutions. Heliyon 10 (18), e37826. https://doi.org/10.1016/j.heliyon.2024.e37826.
Shojaiepour, M., Kharrat, R., Shojaiepour, M., Hashemi, A., 2014. Experimental and simulation study of in-situ combustion process in carbonate fractured porous media. J. Jpn. Pet. Inst. 57, 208–215. https://doi.org/10.1627/jpi.57.208.
Siauciunas, R., Smalakys, G., Dambrauskas, T., 2021. Porosity of calcium silicate hydrates synthesized from natural rocks. Materials (Basel) 14 (19), 5592. https://doi.org/10.3390/ma14195592.
Subbotina, M., Mukhina, E., Karamov, T., Popov, E., Kozlova, E., Morkovkin, A., Mukhametdinova, A., Prochukhan, K., Cheremisin, A., 2023. Evolution of reservoir properties of oil shale rocks under hydro-thermal treatment: Investigations from micro- to macro-scale. Geoenergy Sci. Eng. 228, 211972. https://doi.org/10.1016/j.geoen.2023.211972.
Tao, L., Hu, Z., Xu, Z., Zhang, X., Ding, Y., Wang, C., Chen, D., Li, S., 2024. Experimental investigation of in situ combustion (ISC) in heavy oil thermal recovery. Geoenergy Sci. Eng. 233. https://doi.org/10.1016/j.geoen.2023.212488.
Tian, H., Stephan, D., Lothenbach, B., Lehmann, C., 2021. Influence of foreign ions on calcium silicate hydrate under hydrothermal conditions: A review. Constr. Build. Mater. 301. https://doi.org/10.1016/j.conbuildmat.2021.124071.
Turta, A.T., Chattopadhyay, S.K., Bhattacharya, R.N., Condrachi, A., Hanson, W., 2007. Current status of commercial in situ combustion projects worldwide. J. Can. Pet. Technol. 46. https://doi.org/10.2118/07-11-GE.
Winland, H.D., 1972. Oil accumulation in response to pore size changes, Weyburn field, Saskatchewan. Amoco Production Company Report, No. F72-G-25, 20 p.
Zhou, W., Xue, S., Han, Y., Zheng, C., 2021. Application of stable carbon and hydrogen isotope technology in the determination of gas sources from limestone layers at Shuangliu mine, China. J. Geophys. Eng. 18 (2), 282–290. https://doi.org/10.1093/jge/gxab013.